Naval Oceanographic Office

Stennis Space Center
MS 39522-5001

Technical Report
TR 309
July 1993

TR 309

MAGNETIC FIELD MODELING OF THE NORTHERN JUAN DE FUCA AND EXPLORER PLATES

JOHN M. QUINN
DONALD L. SHIEL

Approved for public release; distribution is unlimited.

Prepared under the authority of
Commander,
Naval Oceanography Command

FOREWORD

The Project MAGNET program, which began in 1951 and which is now more than 40 years old, has primarily been tasked to globally collect high-level, vector aeromagnetic data to support magnetic mapping for navigational purposes. However, the unique remote-sensing capabilities of the Project MAGNET aircraft are only fully realized in low-level applications. In the low-level mode of operations, this aircraft has been tasked to perform mineral resource evaluations in southeast Asia, to evaluate hazards to submarine navigation in remote areas around the world, and even to search for sunken ships. Yet, having the ability to collect high-quality geophysical data sets from unique data acquisition platforms is of little value without also having developed sophisticated analytic tools to extract desired information from the data.

This report, which concerns a low-level Project MAGNET survey of the northern Juan de Fuca and Explorer Plates, a region of intense scientific interest due to its volcanic and tectonic activity and due to its proximity to the west coasts of Canada and the United States, exhibits a generous mixture of both high-quality survey data and sophisticated mathematical and computer analysis. The results of the analyses permit one to peer several kilometers below the bathymetric layer of the ocean to see hidden basalt structures with unusual detail. Occasionally, one of these basalt structures will rise in the form of a seamount well above the usual oceanic sediment coating. It then becomes a hazard to submarine navigation and consequently becomes of interest and concern to the navy.

D J Whitford

D. J. WHITFORD
Commander, U.S. Navy
Commanding Officer
Acting

DISCLAIMER NOTICE

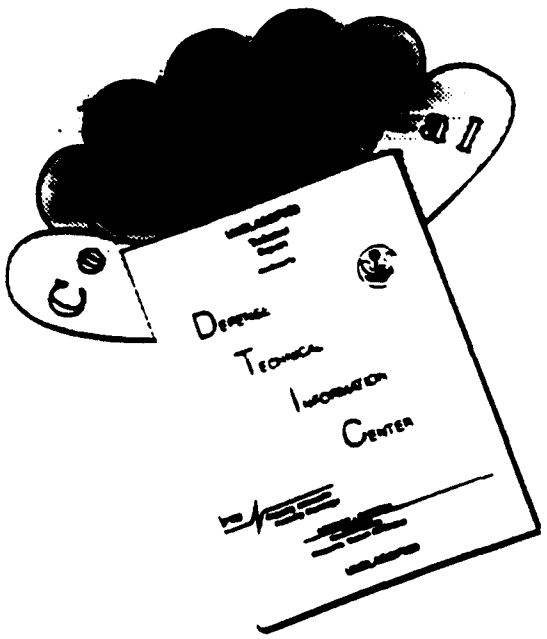

THIS DOCUMENT IS BEST QUALITY AVAILABLE. THE COPY FURNISHED TO DTIC CONTAINED A SIGNIFICANT NUMBER OF COLOR PAGES WHICH DO NOT REPRODUCE LEGIBLY ON BLACK AND WHITE MICROFICHE.

REPORT DOCUMENTATION PAGE

Form Approved
OMB No. 0704-0188

1. AGENCY USE ONLY *(Leave blank)*	2. REPORT DATE	3. REPORT TYPE AND DATES COVERED
	July 1993	Technical Report

4. TITLE AND SUBTITLE

Magnetic Field Modeling of the Northern Juan de Fuca and Explorer Plates

5. FUNDING NUMBERS

6. AUTHOR(S)

John M. Quinn
Donald L. Shiel

7. PERFORMING ORGANIZATION NAME(S) AND ADDRESS(ES)

Commanding Officer
Naval Oceanographic Office
1002 Balch Boulevard
Stennis Space Center, MS 39522-5001

8. PERFORMING ORGANIZATION REPORT NUMBER

TR 309

9. SPONSORING/MONITORING AGENCY NAME(S) AND ADDRESS(ES)

Commander
Naval Oceanography Command
1020 Balch Boulevard
Stennis Space Center, MS 39522-5001

10. SPONSORING/MONITORING AGENCY REPORT NUMBER

NTIS CRA&I ☒
DTIC TAB ☐
Unannounced ☐
Justification .....

11. SUPPLEMENTARY NOTES

By .....
Distribution /
Availability Codes

12a. DISTRIBUTION/AVAILABILITY STATEMENT

Approved for public release; distribution is unlimited.

12b. DISTRIBUTION CODE

Dist	Avail and/or Special
A-1	

13. ABSTRACT *(Maximum 200 words)*

A detailed low-level (500-ft) vector-aeromagnetic survey of the northern Juan de Fuca and Explorer plates, from 47° N to 51° N and from 124° W to 130° W, was conducted by the U.S. Navy's Project MAGNET aircraft in July 1981. The measured vector component data from this survey were used to create a 65,536 coefficient rectangular-harmonic, crustal, magnetic potential-field model for the region. This model, in turn, was used to generate self-consistent, uniformly spaced vector and gradient field grids which, via inverse modeling, were used to estimate magnetic-source-depths and relative magnetizations for the entire survey area at approximately a 1.5-nmi resolution.

14. SUBJECT TERMS

Aeromagnetic surveys, Juan de Fuca, magnetic-field model, Project MAGNET, rectangular-harmonic modeling techniques

15. NUMBER OF PAGES

86

16. PRICE CODE

17. SECURITY CLASSIFICATION OF REPORT	18. SECURITY CLASSIFICATION OF THIS PAGE	19. SECURITY CLASSIFICATION OF ABSTRACT	20. LIMITATION OF ABSTRACT
UNCLASSIFIED	UNCLASSIFIED	UNCLASSIFIED	UL

TABLE OF CONTENTS

Section 1. Introduction 1

Section 2. Data Collection and Reduction Procedures 5

2.1 Instrumentation, Calibration, Environmental Corrections, and Processing 5
2.2 Coordinate Transformations 8

Section 3. The Potential Field Model 12

3.1 The Regional Magnetic-Field Model 13
3.2 The Local Magnetic-Field Model 18
3.2.1 Computing the Local Magnetic-Field Vector from the Model 35
3.2.2 Computing the Magnetic-Gradient Tensor from the Model 38

Section 4. Inverse Modeling (Magnetic Depth-to-Source) 60

Section 5. Comments on Nonuniqueness 86

References 89

LIST OF FIGURES

FIGURE

1. Juan de Fuca Aeromagnetic Survey Design 3

2. Juan de Fuca DBDB5 Bathymetry 4

3a. Juan de Fuca X-Component Magnetic Field 39

3b. Juan de Fuca Y-Component Magnetic Field 41

3c. Juan de Fuca Z-Component Magnetic Field 43

4a. Juan de Fuca XX-Component Magnetic-Field Gradient 49

4b. Juan de Fuca XY-Component Magnetic-Field Gradient 51

4c. Juan de Fuca XZ-Component Magnetic-Field Gradient 53

4d. Juan de Fuca YY-Component Magnetic-Field Gradient 55

4e. Juan de Fuca YZ-Component Magnetic-Field Gradient 57

LIST OF FIGURES (CON.)

FIGURE

4f. Juan de Fuca ZZ-Component Magnetic-Field Gradient 59

5. Juan de Fuca Magnetic-Source-Depth.....69

6a. Juan de Fuca X-Component Magnetization 71

6b. Juan de Fuca Y-Component Magnetization 73

6c. Juan de Fuca Z-Component Magnetization 75

7a. Juan de Fuca Z-Component Magnetization Profile (nT) Along Longitude 129.65W...77

7b. Juan de Fuca Z-Component Magnetization Profile (nT) Along Longitude 129.80W...79

7c. Juan de Fuca Z-Component Magnetization Profile (nT) Along Latitude 47.30N 81

7d. Juan de Fuca Z-Component Magnetization Profile (nT) Along Latitude 48.23N 83

7e. Juan de Fuca Z-Component Magnetization Profile (nT) Along Latitude 48.40N 85

LIST OF TABLES

TABLE

1. Project MAGNET Flights in the Northern Juan de Fuca/Explorer Plate Region..... 6

2. Regional Magnetic Model for the Northern Juan de Fuca/Explorer Plates.....16

3. Regional Magnetic Model for the Northern Juan de Fuca/Explorer Plates: Revision of Table 2 Based on Symmetry Considerations 17

4. Rectangular-Harmonic Model Coefficients of the Juan de Fuca/Explorer Plate Regions, Low Degree and Order Terms Only 22

5. Elements of the Λ Matrix Elements.....64

6. Derivatives of the Λ Matrix Elements.....65

1. INTRODUCTION

The Juan de Fuca and Explorer plates have been extensively surveyed over a period of several decades, primarily using shipborne scalar magnetometers, as noted by Raff and Mason (1961), Elvers et al. (1974), and more recently by Tivey and Johnson (1990). The tectonic evolution of this area is summarized by Botros and Johnson (1988) and by Karsten and Delaney (1989), while the present geomorphological view of the region is summarized by Finn (1990). The most detailed studies of the region have concentrated on the special relationship that exists between the Axial and Cobb seamounts and the Juan de Fuca Ridge. This relationship is described from the magnetic viewpoint by Tivey and Johnson (1990), from the bathymetric viewpoint via Sea Marc I data by Applegate (1990), from the chemical viewpoint by Rhodes et al. (1990), from the gravity viewpoint by Hildebrand et al. (1990), and from the seismic reflection and refraction viewpoints by Morton et al. (1987) and by White and Clowes (1990). The subduction of the Juan de Fuca plate under the western continental margin of the North American Plate has been studied as far east as the Washington and Oregon Cascade Mountain Range, using teleseismic P-wave tomographic imaging techniques, accounts of which are given by Rasmussen and Humphreys (1988) and by Harris, Iyer, and Dawson (1991).

The original purpose for the analysis being presented here was to develop a practical method of identifying hazards to underwater navigation for the U.S. Navy, using magnetic techniques that take advantage of the Navy's unique aeromagnetic survey resource, the Project MAGNET RP-3D Orion aircraft. The Project MAGNET program originated in 1951. During the program's lifetime, several aircraft have been used (Coleman, 1992). The current aircraft has the unique capability of performing large-scale vector aeromagnetic surveys in remote ocean areas in relatively short time spans. The Juan de Fuca area provided a sufficiently geologically

complicated morphology to test the robustness of any method that might be developed. The most prominent hazard is the seamount. The basic assumption is that most of these seamounts are volcanic in origin and therefore are composed of basalt materials that have strong magnetic properties. The Juan de Fuca survey area includes the Heck seamount chain, the Juan de Fuca Ridge, the Endeavor Segment, and the Explorer Ridge, all of which are volcanic in origin.

Because the aircraft provides vector magnetic measurements, it is an easy matter to produce a rectangular-harmonic magnetic potential-field model from survey data which have been collected at a single altitude. After appropriate data reduction these data can be gridded and subsequently transformed from geodetic to rectangular coordinates, where the data is then amenable to Fast Fourier Transform (FFT), rectangular-harmonic modeling techniques, which will subsequently be described. Technical aspects of rectangular-harmonic analysis are discussed by Alldredge (1981, 1982). However, our methods and procedures are somewhat different than his.

The model presented here is derived from survey data collected during a detailed, low-level (500-ft), U.S. Navy Project MAGNET, vector-aeromagnetic survey performed during the months of August and September 1981. This survey covers the ocean area bounded from 47^0 N to 51^0 N and from 124^0 W to 130^0 W as indicated in Figure 1. The corresponding bathymetry for this region, taken from the 5-minute gridded data base DBDB5, is shown in Figure 2. The model, in turn, is used to recompute the magnetic vector-component grids from which the model is derived and to compute as well, the magnetic gradient-tensor component grids of the region. These magnetic vector and gradient-tensor components are combined via an inverse-modeling technique which employs the concept of uniformly magnetized rectangular prisms to estimate the magnetic depth-to-source for the entire surveyed region. As a by-product the relative

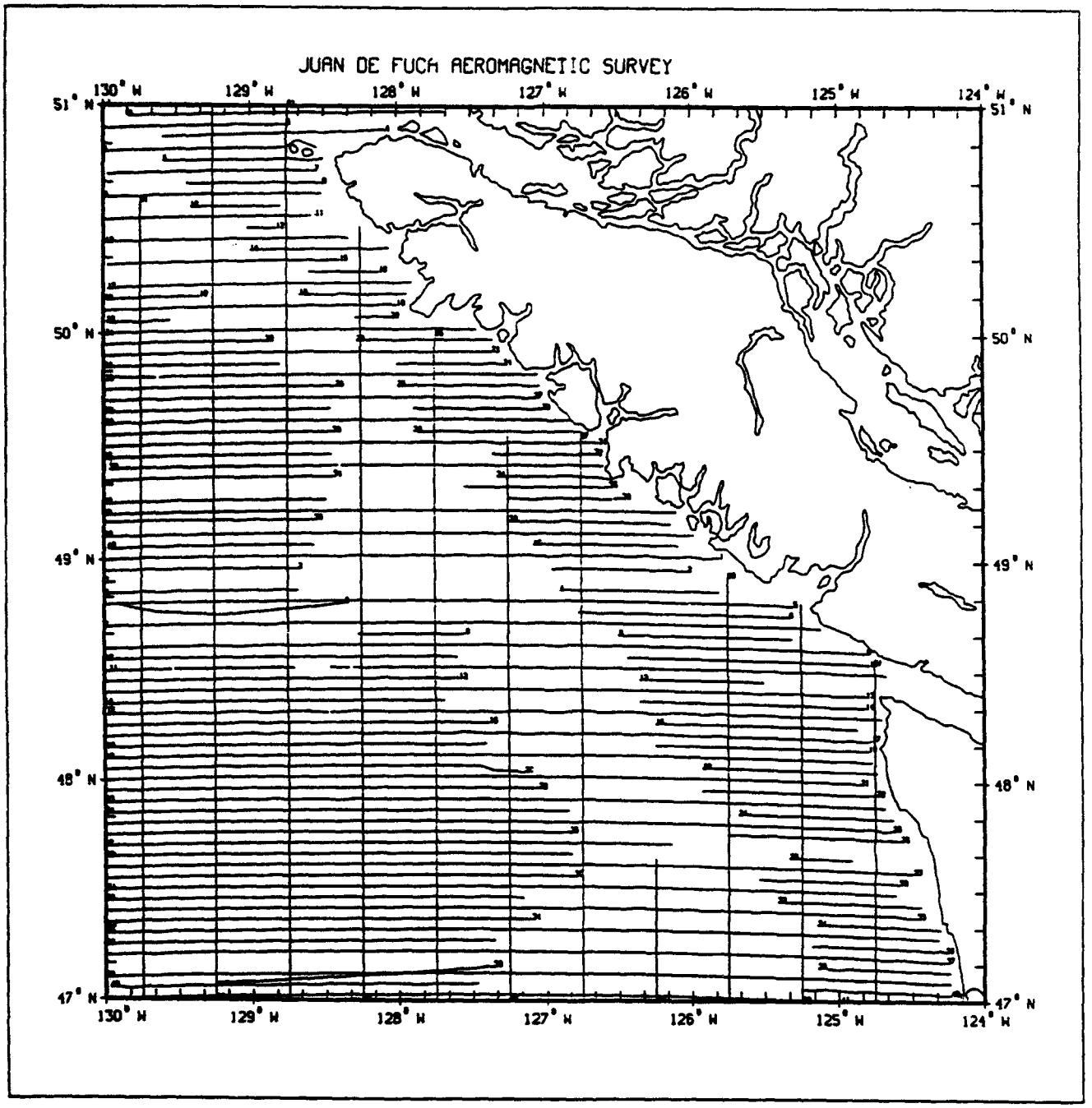

Figure 1. Juan de Fuca Aeromagnetic Survey Design; Altitude: 500-ft

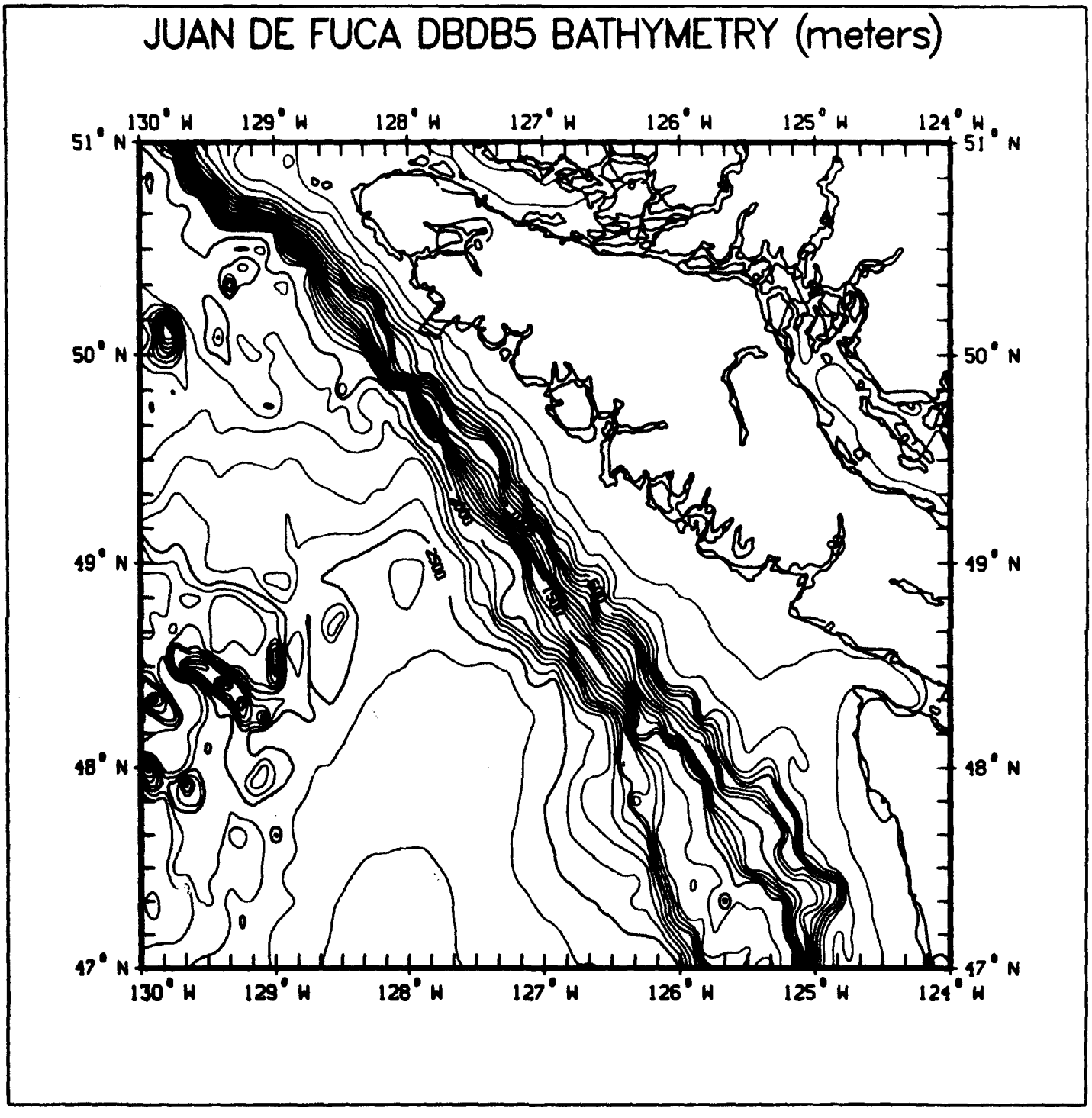

Figure 2. Juan de Fuca DBDB5 Bathymetry; Units: meters

magnetic morphology (i.e., the magnetization distribution) of the region is also estimated. The rectangular-prism, inverse-modeling technique employed in this study has a long history with many variations. The variation used here is described in detail by Quinn and Shiel (1993). This technique does not distinguish between remnant magnetization and induced magnetization.

2. DATA COLLECTION AND REDUCTION PROCEDURES

The Juan de Fuca survey was conducted during the months of August and September 1981. The actual dates flown are given in Table 1 along with the project identification and the flight numbers. These identifications are attached to the data sets by the Naval Oceanographic Office, which conducted these surveys in cooperation with the Navy's P3 squadron VXN-8, located at Patuxent River Naval Air Station, Patuxent River, Maryland. Additional Project MAGNET flights in the Juan de Fuca area were conducted in 1980 and 1983. These flights were not used in this study but are nevertheless listed in Table 1 as a matter of completeness for the benefit of future studies.

2.1 Instrumentation, Calibration, Environmental Corrections, and Processing

The 1981 survey was conducted at an altitude of 500 feet, as determined by a precision Rosemont Barometric Altimeter used by the pilot. The densely spaced East-West survey tracks were separated by 3 nmi except in a magnetically quiet zone located over the trench, adjacent to the continental shelf, where the spacing was increased to 6 nmi. Survey tracks flown for control purposes in the North-South direction were separated by 20 nmi. The effective along-track sample rate was 0.5 Hertz, while the speed of the aircraft was approximately 240 nmi per hour. Magnetograms from a nearby geomagnetic observatory at Victoria, British Columbia, were used

Table 1. Project MAGNET Flights in the Northern Juan de Fuca/Explorer Plate Regions

Project #	Flight #	Year	Month	Day	Senior Scientists
A32 - 053	9102	1980	April	23	Jesus Anglero, Charles Gunn & Mike Anderson
A32 - 053	9103	1980	April	25	
A32 - 154	9411	1981	August	3	Donald Wilson, Jesus Anglero & Steve Feldman
A32 - 154	9412	1981	August	5	
A32 - 154	9366	1981	August	7	"
A32 - 154	9367	1981	August	10	"
A32 - 154	9413	1981	August	12	"
A32 - 154	9414	1981	August	14	"
A32 - 154	9418	1981	September	3	"
C32 - 451	9429	1983	November	9	Virgil Bettencourt & Donald Wilson
C32 - 451	9430	1983	November	11	"
C32 - 451	9431	1983	November	16	"

to monitor and remove short-term (i.e., < 2 months) temporal magnetic variations. The most prominent contribution to these short-term temporal variations is the Solar quiet (Sq) Daily Variation (DV) of the geomagnetic field and its corresponding induction field. Campbell, Schiffmacher and Kroehl (1989) have globally modeled the Sq variations. Their model is now available from the National Geophysical Data Center which is located in Boulder, Colorado. These Sq magnetic variations, the ionospheric currents that generate them, and the corresponding induced magnetic fields from the Earth's conducting crust and upper mantle are described in some detail by Campbell and Schiffmacher (1988a, 1988b) and by Campbell (1989a, 1989b).

Data from the magnetic observatory were also used to calibrate the vector magnetometer and to compensate for aircraft-generated magnetic fields. Typical Project MAGNET calibration/compensation procedures, which involve airswings over magnetic observatories, are described by Coleman (1992). A portable Vector Magnetic Ground Station (VMGS) was established at McChord Air Force Base near Tacoma, Washington, also for the purpose of eliminating temporal variations from the data. The typical 11- to 12-hour flights were conducted at night to further reduce the effect of temporal magnetic variations generated by ionospheric and magnetospheric current systems and their corresponding crustal induction effects.

Navigation and attitude were determined using the Navy doppler radar satellite navigation system and a redundant set of three inertial navigation/attitude systems. The RMS navigation error is estimated to be on the order of .1 nmi RMS, while the attitude errors for Yaw, Pitch, and Roll are estimated to be on the order of 1 arc-minute RMS. These data, like the magnetics data, require extensive editing for spurious noise spikes, drift corrections, and time syncing.

Generally, the recorded time is accurate to within a few milliseconds. The Juan de Fuca survey took place prior to the deployment of the Global Positioning System (GPS). So, GPS navigation was not available.

Having reduced the data for each flight, the Main (core-generated) magnetic field was removed using the 1980 Epoch, Degree 13 Spherical-Harmonic Model (GSFC 12/83) of Langel nd Estes (1985), which is based on MAGSAT data. The residual X, Y, and Z magnetic field components are then essentially of crustal origin. Data for each magnetic component were gridded separately and interpolated as necessary, into lat x lon cells of 1.5 arc-minutes x 1.5 arc-minutes (i.e., roughly half of the East-West track spacing) such that each component consists of 256 x 256 grid points. The Project MAGNET survey covered only ocean areas. It did not extend beyond the coastline to the adjacent continental land area. So, the extreme east and northeast portions of the grid were zero filled in such a way as to allow interpolation of the magnetic residuals over the land areas from the coastline to the edge of the grid to smoothly taper off to zero, thus avoiding later problems with Gibbs phenomena. The gridding process also has the advantage of smoothing out instrument noise, navigational errors, and other environmentally generated fields, not of crustal origin, that cannot otherwise be accounted for and thus eliminated.

2.2 Coordinate Transformations

When the three magnetic-component residual grids are considered as a single vector unit, each grid point has associated with it X-, Y-, and Z-component magnetic-field values which are first transformed from geodetic to spherical coordinates (Cain et. al., 1967) and subsequently from spherical to rectangular coordinates (Alldredge, 1981). These two

procedures involve not just coordinate transformations at the site of each grid point, but also rotations of the residual magnetic-field vector at each grid point.

The geodetic position (i.e., latitude, longitude, and altitude) of a data point is denoted as (λ,φ,h). The same position referenced to spherical coordinates, corresponding to the geocentric radius, the colatitude, and the longitude is denoted as (r,θ,φ). So, in geodetic coordinates, the residual magnetic-field vector components, corresponding to X-North, Y-East, and Z-Vertically Down, which forms a right-handed system, are denoted as $B_x(\lambda,\varphi,h)$, $B_y(\lambda,\varphi,h)$, and $B_z(\lambda,\varphi,h)$. Prior removal of the Main field at the mean survey epoch of 1981.2 using the GSFC 12/83 model and removal of the short-term temporal variations using the observatory data eliminates the time dependence from the residual data sets. The same residual magnetic-field vector-component values referenced to spherical coordinates have radial, colatitudinal, and longitudinal components denoted as $B_r(r,\theta,\varphi)$, $B_\theta(r,\theta,\varphi)$, and $B_\varphi(r,\theta,\varphi)$. Using this notation, the geodetic to spherical coordinate transformation used at each grid point of each of the three vector-component grids is as follows:

$$\cos\theta = \frac{\sin\lambda}{\sqrt{Q^2\cos^2\lambda + \sin^2\lambda}} \tag{1a}$$

$$\sin\theta = \sqrt{1 - \cos^2\theta} \tag{1b}$$

$$Q = \frac{h\sqrt{a^2-(a^2-b^2)\sin^2\lambda} + a^2}{h\sqrt{a^2-(a^2-b^2)\sin^2\lambda} + b^2} \tag{1c}$$

$$r^2 = h^2 + 2h\sqrt{a^2 - (a^2-b^2)\sin^2\lambda} + \frac{a^4-(a^4-b^4)\sin^2\lambda}{a^2-(a^2-b^2)\sin^2\lambda} \tag{1d}$$

$$\varphi = \varphi \tag{1e}$$

where, the parameters a and b are the semi-major and semi-minor axes of the ellipsoid to which the geodetic coordinates are referenced. In the case of the Juan de Fuca survey, the reference ellipsoid was that corresponding to the World Geodetic System 1972 (WGS-72). The corresponding magnetic-field vector-component rotation from geodetic to spherical coordinates is:

$$B_r(r, \theta, \varphi) = \sin\alpha\, B_x(\lambda, \varphi, h) + \cos\alpha\, B_z(\lambda, \varphi, h) \tag{2a}$$

$$B_\theta(r, \theta, \varphi) = -\cos\alpha\, B_x(\lambda, \varphi, h) + \sin\alpha\, B_z(\lambda, \varphi, h) \tag{2b}$$

$$B_\varphi(r, \theta, \varphi) = B_y(\lambda, \varphi, h) \tag{2c}$$

where the rotation angle α is defined as:

$$\alpha = \lambda + \theta - \frac{\pi}{2} \tag{3}$$

and where θ is computed from eq. (1a). Equivalently, the angle α may be defined by the following convenient relations:

$$\sin\alpha = \frac{(a^2 - b^2)\sin\lambda\cos\lambda}{r\sqrt{a^2\cos^2\lambda + b^2\sin^2\lambda}} \tag{4a}$$

$$\cos\alpha = \frac{h + \sqrt{a^2\cos^2\lambda + b^2\sin^2\lambda}}{r} \tag{4b}$$

The subsequent transformation from spherical coordinates (r,θ,φ) to rectangular coordinates (x,y,z) assumes that there is a plane tangent to the sphere with its origin at the point (R,θ_0,φ_0), where R is the mean radius of the Earth as determined by the parameters of the reference ellipsoid, while θ_0 and φ_0 define the center of the survey area in spherical coordinates.

The rectangular coordinate-system axes are oriented with respect to the spherical coordinate system such that the X-axis points north, in the direction of $-\theta$, the Y-axis points east in the direction of $+\varphi$, and the Z-axis points vertically down in the direction of -r, thus making a right-handed system. Consequently, the transformation from spherical coordinates to rectangular coordinates takes the following mathematical form:

$$x = r \sin\Psi \cos\Upsilon \tag{5a}$$

$$y = r \sin\Psi \sin\Upsilon \tag{5b}$$

$$z = R - r \cos\Psi \tag{5c}$$

where:

$$\Psi = \cos^{-1}[\cos\theta_0 \cos\theta + \sin\theta_0 \sin\theta \cos(\varphi - \varphi_0)] \tag{6a}$$

$$\Upsilon = \sin^{-1}\left[\frac{\sin\theta \sin(\varphi - \varphi_0)}{\sin\Psi}\right] \tag{6b}$$

and where:

$$\cos\Upsilon = +\sqrt{1 - \sin^2\Upsilon} \qquad |\Upsilon| \leq 90^0 \tag{7a}$$

$$\cos\Upsilon = -\sqrt{1 - \sin^2\Upsilon} \qquad |\Upsilon| > +90^0 \tag{7b}$$

The corresponding rotation of the magnetic-field vector components is:

$$B_x(x,y,z) = -B_x' \cos\theta_0 \cos\varphi_0 - B_y' \cos\theta_0 \sin\varphi_0 + B_z' \sin\theta_0 \tag{8a}$$

$$B_y(x,y,z) = -B_x' \sin\varphi_0 + B_y' \cos\varphi_0 \tag{8b}$$

$$B_z(x,y,z) = -B_x' \sin\theta_0 \cos\varphi_0 - B_y' \sin\theta_0 \sin\varphi_0 - B_z' \cos\theta_0 \tag{8c}$$

where:

$$B_x' = B_\theta \cos\theta \cos\varphi - B_\varphi \sin\varphi + B_r \sin\theta \cos\varphi \tag{9a}$$

$$B_y' = B_\theta \cos\theta \sin\varphi + B_\varphi \cos\varphi + B_r \sin\theta \sin\varphi \tag{9b}$$

$$B_z' = -B_\theta \sin\theta + B_r \cos\theta \tag{9c}$$

After performing these transformations, the resulting gridded magnetic-field components are suitable for rectangular-harmonic analysis.

3. THE POTENTIAL FIELD MODEL

The three residual grids corresponding to the three magnetic-field components of the Juan de Fuca area are presumed to be related to each other through a single magnetic potential V(x,y,z). This potential is composed of two parts, a regional potential $V_R(x,y,z)$ and a local potential

$V_L(x,y,z)$ so that:

$$V(x,y,z) = V_R(x,y,z) + V_L(x,y,z) \tag{10}$$

The regional potential $V_R(x,y,z)$ includes magnetic-field contributions generated in the Earth's fluid core and contributions generated by induced and remnant magnetization originating in the deeper crust above the Curie depth. The regional magnetic potential has characteristic wavelengths that are longer than the dimensions of the survey area. The local potential $V_L(x,y,z)$ on the other hand is presumed to be due to Main field induced and remnant magnetizations originating in the Earth's upper crust and has characteristic wavelengths on the order of or shorter than the dimensions of the survey area, which is taken to be rectangular with dimensions L_x x L_y . From these lengths, a single characteristic dimension L of the survey area can be defined as:

$$L = \sqrt{L_x L_y} \tag{11}$$

In the case of the Juan de Fuca survey, L_x = 664.466 kilometers, while L_y = 428.406 kilometers so that L = 533.537 kilometers.

3.1 The Regional Magnetic-Field Model

The regional magnetic-field potential is taken to be of the following quadratic form:

$$V_R(x,y,z) = a_\mu x^\mu + \tfrac{1}{2} b_{\mu\nu} x^\mu x^\nu \qquad \mu,\nu = 1,2,3 \tag{12}$$

where tensor notation has been used in which the coordinates (x,y,z) correspond to (x^1,x^2,x^3) and where Einstein summation notation is used so that repeated indices are to be summed over. Thus, for instance:

$$a_\mu x^\mu \equiv a_1 x^1 + a_2 x^2 + a_3 x^3 = a_1 x + a_2 y + a_3 z \tag{13}$$

Using the single slash (/) notation (Adler, Bazin, and Schiffer [1975]) to denote partial differentiation, so that for instance ($/\mu \equiv \frac{\partial}{\partial x^\mu}$), the regional magnetic field $B_R(x,y,z)$, which is the negative gradient of the regional potential, may be computed as:

$$B_{R\mu}(x,y,z) = -V_{R/\mu}(x,y,z) = -a_\mu - b_{\mu\nu}x^\nu \tag{14}$$

It thus becomes clear that the constants $-a_\mu$ are the regional mean values of the corresponding magnetic-field components. The local magnetic field will therefore have a zero mean for each of its magnetic components. Subsequently, taking the positive gradient of the regional magnetic field yields the regional magnetic gradient tensor:

$$\mathcal{B}_{R\mu\nu}(x,y,z) = B_{R\mu/\nu}(x,y,z) = -b_{\mu\nu} \tag{15}$$

Thus, it is clear that the nine constant coefficients $-b_{\mu\nu}$ correspond to the average gradient or slope over the entire survey area of each of the three magnetic components in each of the three coordinate directions.

Since the regional magnetic gradient is obtained by taking two gradients of the regional magnetic potential and since the order in which these gradients are performed is of no consequence, the regional magnetic-gradient tensor must be symmetric. Also, since the regional

magnetic potential must satisfy Laplace's equation, the regional magnetic-gradient tensor must also have zero trace. So, this tensor has only five independent components and the coefficients $b_{\mu\nu}$ satisfy the following symmetry conditions:

$$b_{\mu\nu} = b_{\nu\mu} \tag{16a}$$

$$b_{\mu}{}^{\mu} = 0 \tag{16b}$$

Experimentally, due to noise and other experimental factors, these relations are never exactly satisfied. The values obtained via least-squares fitting for the regional magnetic biases a_{μ} and the regional magnetic gradients $b_{\mu\nu}$ for the Juan de Fuca area are listed in Table 2. Note that the vertical gradients were not measured since this would have required a second identical survey at a second altitude. However, these gradients may be inferred from the information in Table 2 using the symmetry conditions above. Note also that due to noise and other measurement errors, the b_{12} coefficient is not identical to b_{21}, so that eq. (16a) is not completely satisfied. However, the average of these two quantities may be taken as the best estimate for both. Table 3 is the appropriate revision of Table 2, which does satisfy all of the symmetry relations for the regional field.

The regional magnetic field, as determined from eq. (12) and the coefficients in Table 2, was removed from the three gridded magnetic-field component data sets that magnetically characterize the Juan de Fuca/Explorer plate regions. The resulting residual grids then define the local magnetic behavior of the combined regions.

Table 2. Regional Magnetic Model for the Northern Juan de Fuca/Explorer Plates

Parameter	Units	Value
L_x	km	664.4660
L_y	km	428.4060
L	km	533.5370
z_o	km	5.3890
a_1	nT	-32.3719
a_2	nT	14.2246
a_3	nT	14.1783
b_{11}	nT/km	0.1401
b_{12}	nT/km	0.1589
b_{13}	nT/km	-----
b_{21}	nT/km	-0.0280
b_{22}	nT/km	-0.0509
b_{23}	nT/km	-----
b_{31}	nT/km	-0.0261
b_{32}	nT/km	-0.1225
b_{33}	nT/km	-----

Table 3. Regional Magnetic Model for the Northern Juan de Fuca/Explorer Plates: Revision of Table 2 Based on Symmetry Considerations

Parameter	Units	Value
L_x	km	664.4660
L_y	km	428.4060
L	km	533.5370
z_s	km	5.3890
a_1	nT	-32.3719
a_2	nT	14.2246
a_3	nT	14.1783
b_{11}	nT/km	0.1401
b_{12}	nT/km	0.0654
b_{13}	nT/km	-0.0261
b_{21}	nT/km	0.0654
b_{22}	nT/km	-0.0509
b_{23}	nT/km	-0.1225
b_{31}	nT/km	-0.0261
b_{32}	nT/km	-0.1225
b_{33}	nT/km	-0.0892

3.2 The Local Magnetic-Field Model

It is now assumed that the regional trends and biases have been removed from the gridded survey data. The local potential-field model is then taken to be the solution of Laplace's equation in rectangular coordinates and may be written in the following form:

$$V_L(x,y,z) = \frac{L}{2\pi} \sum_{n=1}^{N} \sum_{m=1}^{M} [A_{nm} \cos n\theta(x) \cos m\varphi(y) + B_{nm} \cos n\theta(x) \sin m\varphi(y) + D_{nm} \sin n\theta(x) \cos m\varphi(y) + E_{nm} \sin n\theta(x) \sin m\varphi(y)] e^{k_{nm} z} \quad (17)$$

where, for a rectangular area of dimensions L_x x L_y :

$$\theta(x) = \frac{2\pi x}{L_x} \qquad -\frac{L_x}{2} \le x \le +\frac{L_x}{2} \quad (18a)$$

$$\varphi(y) = \frac{2\pi y}{L_y} \qquad -\frac{L_y}{2} \le y \le +\frac{L_y}{2} \quad (18b)$$

and where the wavenumber k_{nm} is given by the relation:

$$k_{nm} = 2\pi \sqrt{\left(\frac{n}{L_x}\right)^2 + \left(\frac{m}{L_y}\right)^2} \qquad 1 \le n \le N; \quad 1 \le m \le M \quad (19)$$

The parameters N and M were both assigned the value of 128 in anticipation of the subsequent use of the 2-dimensional FFT, while the parameter L was previously defined by eq. (11).

The objective is to determine the rectangular-harmonic coefficients A_{nm}, B_{nm}, D_{nm}, and E_{nm}, which are real-valued constants with units of nanoTeslas (nT), using the gridded, residual magnetic-field vector components derived from the survey data. These magnetic-field

components are related to the negative gradients of the local magnetic potential defined by eq. (17), so that:

$$\mathbf{B}_L(x,y,z) = -\nabla V_L(x,y,z) \tag{20}$$

Consequently, the three residual magnetic-field components may be expressed as follows:

$$B_{Lx}(x,y,z) = +\frac{L}{L_x}\sum_{n=1}^{N}\sum_{m=1}^{M} n[A_{nm}\sin n\theta(x)\cos m\varphi(y) + B_{nm}\sin n\theta(x)\sin m\varphi(y) - D_{nm}\cos n\theta(x)\cos m\varphi(y) - E_{nm}\cos n\theta(x)\sin m\varphi(y)]e^{k_{nm}z} \tag{21a}$$

$$B_{Ly}(x,y,z) = +\frac{L}{L_y}\sum_{n=1}^{N}\sum_{m=1}^{M} m[A_{nm}\cos n\theta(x)\sin m\varphi(y) - B_{nm}\cos n\theta(x)\cos m\varphi(y) + D_{nm}\sin n\theta(x)\sin m\varphi(y) - E_{nm}\sin n\theta(x)\cos m\varphi(y)]e^{k_{nm}z} \tag{21b}$$

$$B_{Lz}(x,y,z) = -\frac{L}{2\pi}\sum_{n=1}^{N}\sum_{m=1}^{N} k_{nm}[A_{nm}\cos n\theta(x)\cos m\varphi(y) + B_{nm}\cos n\theta(x)\sin m\varphi(y) + D_{nm}\sin n\theta(x)\cos m\varphi(y) + E_{nm}\sin n\theta(x)\sin m\varphi(y)]e^{k_{nm}z} \tag{21c}$$

For convenience in the following discussion, the subscript L will be suppressed, and it will be assumed from this point onward that we are concerned with the local magnetic potential and the local fields and gradients that can be derived from it. We then proceed by noting that the rectangular-harmonic coefficients of the local magnetic potential can be computed from any one of the three gridded components of the geomagnetic residual field, which are presumed to have

been measured at some nearly constant survey altitude, H, (i.e., z = -H) above the x-y plane. If the X-component of the residual magnetic field is used, then, using the usual orthogonality conditions for the sine and cosine functions, these coefficients are determined as follows:

$$A_{nm} = + \frac{L_x}{n\pi^2 L} e^{k_{nm}H} \int_{-\pi}^{\pi}\int_{-\pi}^{\pi} \sin n\theta \cos m\varphi \, B_x(\theta, \varphi, -H)\, d\theta\, d\varphi \qquad (22a)$$

$$B_{nm} = + \frac{L_x}{n\pi^2 L} e^{k_{nm}H} \int_{-\pi}^{\pi}\int_{-\pi}^{\pi} \sin n\theta \sin m\varphi \, B_x(\theta, \varphi, -H)\, d\theta\, d\varphi \qquad (22b)$$

$$D_{nm} = - \frac{L_x}{n\pi^2 L} e^{k_{nm}H} \int_{-\pi}^{\pi}\int_{-\pi}^{\pi} \cos n\theta \cos m\varphi \, B_x(\theta, \varphi, -H)\, d\theta\, d\varphi \qquad (22c)$$

$$E_{nm} = - \frac{L_x}{n\pi^2 L} e^{k_{nm}H} \int_{-\pi}^{\pi}\int_{-\pi}^{\pi} \cos n\theta \sin m\varphi \, B_x(\theta, \varphi, -H)\, d\theta\, d\varphi \qquad (22d)$$

Alternatively, using the Y-component magnetic residuals, these coefficients are determined as:

$$A_{nm} = + \frac{L_y}{m\pi^2 L} e^{k_{nm}H} \int_{-\pi}^{\pi}\int_{-\pi}^{\pi} \cos n\theta \sin m\varphi \, B_y(\theta, \varphi, -H)\, d\theta\, d\varphi \qquad (23a)$$

$$B_{nm} = - \frac{L_y}{m\pi^2 L} e^{k_{nm}H} \int_{-\pi}^{\pi}\int_{-\pi}^{\pi} \cos n\theta \cos m\varphi \, B_y(\theta, \varphi, -H)\, d\theta\, d\varphi \qquad (23b)$$

$$D_{nm} = + \frac{L_y}{m\pi^2 L} e^{k_{nm}H} \int_{-\pi}^{\pi}\int_{-\pi}^{\pi} \sin n\theta \sin m\varphi \, B_y(\theta, \varphi, -H)\, d\theta\, d\varphi \qquad (23c)$$

$$E_{nm} = - \frac{L_y}{m\pi^2 L} e^{k_{nm}H} \int_{-\pi}^{\pi}\int_{-\pi}^{\pi} \sin n\theta \cos m\varphi \, B_y(\theta, \varphi, -H)\, d\theta\, d\varphi \qquad (23d)$$

The third alternative uses the Z-component of the residual magnetic field and yields the following expressions for these coefficients:

$$A_{nm} = -\frac{2}{\pi L k_{nm}} e^{k_{nm}H} \int_{-\pi}^{\pi}\int_{-\pi}^{\pi} \cos n\theta \cos m\varphi \, B_z(\theta, \varphi, -H)\, d\theta\, d\varphi \tag{24a}$$

$$B_{nm} = -\frac{2}{\pi L k_{nm}} e^{k_{nm}H} \int_{-\pi}^{\pi}\int_{-\pi}^{\pi} \cos n\theta \sin m\varphi \, B_z(\theta, \varphi, -H)\, d\theta\, d\varphi \tag{24b}$$

$$D_{nm} = -\frac{2}{\pi L k_{nm}} e^{k_{nm}H} \int_{-\pi}^{\pi}\int_{-\pi}^{\pi} \sin n\theta \cos m\varphi \, B_z(\theta, \varphi, -H)\, d\theta\, d\varphi \tag{24c}$$

$$E_{nm} = -\frac{2}{\pi L k_{nm}} e^{k_{nm}H} \int_{-\pi}^{\pi}\int_{-\pi}^{\pi} \sin n\theta \sin m\varphi \, B_z(\theta, \varphi, -H)\, d\theta\, d\varphi \tag{24d}$$

Generally, the magnetic residual component exhibiting the largest amplitude is the preferred one for computing the rectangular-harmonic coefficients. This choice will yield smaller coefficient errors due to the smaller percentage of noise intrinsic to the data for that magnetic component relative to the others. The Z-component grid was chosen for this purpose in the Juan de Fuca/Explorer region. The resulting coefficients are partially listed to degree 15 in Table 4.

Evaluation of the above expressions for the rectangular-harmonic coefficients is accomplished with the aid of the 2-dimensional FFT. First, note that each residual, magnetic-component grid can be represented in the form of a 2-dimensional, finite Fourier series as follows:

$$B_x(\theta, \varphi, -H) = \sum_{\nu=-N}^{N} \sum_{\mu=-M}^{M} b_{x\nu\mu}(-H)\, e^{i(\nu\theta + \mu\varphi)} \tag{25a}$$

$$B_y(\theta, \varphi, -H) = \sum_{\nu=-N}^{N} \sum_{\mu=-M}^{M} b_{y\nu\mu}(-H)\, e^{i(\nu\theta + \mu\varphi)} \tag{25b}$$

Table 4. Rectangular-Harmonic Model Coefficients of the Juan de Fuca/Explorer Plate Regions, Low Degree and Order Terms Only; Units: nanoTeslas

n	m	A_{nm}	B_{nm}	D_{nm}	E_{nm}
1	1	-6.50182	0.90794	10.10035	6.98122
1	2	-4.20178	-4.19915	-8.77588	1.38671
1	3	-0.17999	2.12747	2.20755	2.62100
1	4	-0.26331	-3.23829	0.96876	-1.44732
1	5	-2.97880	-0.39970	-1.28883	-1.16297
1	6	0.24739	1.26363	-1.31373	0.99827
1	7	0.07261	-0.82978	0.78405	0.23625
1	8	-0.19026	0.76457	-0.15335	0.17747
1	9	0.16159	-0.28253	0.38965	-0.44789
1	10	-0.51639	0.44997	-0.63982	-0.07680
1	11	0.16159	0.12405	0.04508	-0.06916
1	12	-0.51639	0.10945	-0.34906	-0.34367
1	13	0.05547	0.09868	-0.18891	0.07211
1	14	-0.32374	0.08613	-0.04772	0.05725
1	15	-0.03293	-0.11430	-0.03724	0.07085
2	1	15.71674	17.28025	18.39594	-5.71595
2	2	-2.36503	-4.43721	-0.32715	7.12863
2	3	-1.61875	-0.47278	-0.32715	-4.94449
2	4	-0.99136	-1.33616	0.32225	2.52737

Table 4. Rectangular-Harmonic Model Coefficients (con.)

2	5	-0.75027	-0.20994	-2.13968	0.08772
2	6	-0.53263	-0.76496	-0.98668	-0.80986
2	7	-0.60334	0.69700	-0.08925	0.71491
2	8	0.22274	0.13464	0.32046	-0.32020
2	9	0.06444	-0.35671	-0.00394	0.16452
2	10	0.00910	-0.42301	0.58391	-0.04872
2	11	-0.23317	-0.44016	0.12173	-0.23388
2	12	0.03802	-0.16201	0.19692	0.22992
2	13	-0.04182	-0.24281	0.26783	-0.10191
2	14	-0.20038	0.05171	-0.05880	-0.09223
2	15	-0.02496	0.16278	0.00662	0.04175
3	1	14.69034	6.64214	26.20008	-6.60164
3	2	-6.92724	-1.22531	0.75517	-3.78142
3	3	-1.85056	-1.13347	-0.55870	0.53041
3	4	-0.58444	0.98213	-0.29600	-1.29544
3	5	0.07912	1.05613	-1.77336	-0.00432
3	6	0.39846	0.04386	0.10321	1.21775
3	7	-0.08147	-0.52859	0.56867	0.05593
3	8	-0.11638	-0.16341	0.51915	-0.13795
3	9	-0.39917	0.27863	-0.31902	-0.17071
3	10	0.41564	0.78612	-0.43821	0.49178

Table 4. Rectangular-Harmonic Model Coefficients (con.)

3	11	0.50470	0.05392	0.02390	0.44870
3	12	0.07068	0.23216	-0.07872	0.03265
3	13	0.20408	0.00148	-0.11725	0.17782
3	14	-0.05528	-0.08068	0.24916	0.06604
3	15	0.03076	0.05477	-0.00173	-0.22982
4	1	-6.72438	5.38535	2.12106	-10.24770
4	2	-1.76723	2.90900	7.01444	0.53800
4	3	-0.40940	0.64107	-0.80526	-0.26738
4	4	-0.65961	-1.39914	-0.59056	-0.91643
4	5	-0.88687	0.32765	-0.42612	-0.86223
4	6	0.43625	-0.16263	-0.17006	-0.43458
4	7	-0.66605	0.63265	-0.45634	0.21541
4	8	0.65868	0.08300	0.04932	0.22266
4	9	-0.35682	-0.32375	0.06753	0.00346
4	10	-0.31478	0.00122	0.24568	-0.32948
4	11	-0.22759	0.11451	-0.23232	-0.43214
4	12	0.05813	-0.13130	0.02407	-0.02362
4	13	-0.18008	-0.01142	-0.00368	-0.20583
4	14	0.15060	0.10593	-0.10623	0.06501
4	15	-0.02681	-0.15914	0.02728	-0.00179
5	1	-9.30405	-2.29585	0.19474	-11.34965

Table 4. Rectangular-Harmonic Model Coefficients (con.)

5	2	3.86618	1.33161	0.43339	-1.80079
5	3	-1.41536	1.66478	-0.85717	1.08008
5	4	1.02127	-1.91231	0.59884	1.66993
5	5	-1.18006	-0.42611	0.38220	-0.17926
5	6	0.42373	-0.07830	-0.19304	0.17104
5	7	-0.71082	-0.53879	0.81771	-0.81005
5	8	-0.32892	0.48116	-0.34766	-0.26324
5	9	0.04880	0.48425	-0.18618	0.12710
5	10	0.66700	0.13226	-0.01505	0.66169
5	11	0.06542	-0.41894	0.38528	0.12194
5	12	-0.10911	0.17215	-0.08716	0.02790
5	13	0.12715	0.01377	0.00680	-0.00514
5	14	-0.02725	-0.00738	-0.12867	0.05027
5	15	0.08473	0.01906	0.06906	0.12909
6	1	-1.28958	-1.31317	-1.35462	-0.85454
6	2	2.25894	-2.98705	-1.59060	2.22455
6	3	-1.39635	2.90327	2.18386	-2.61767
6	4	1.09335	0.01516	-1.91373	1.55669
6	5	-0.43473	0.33791	0.72297	0.51169
6	6	0.02327	-0.55756	-0.15552	-0.28759
6	7	0.03012	0.38200	-0.19865	0.46374

Table 4. Rectangular-Harmonic Model Coefficients (con.)

6	8	0.67396	-0.27972	0.42758	0.19033
6	9	-0.40740	-0.34895	0.14588	-0.70268
6	10	-0.23443	0.20503	-0.43304	-0.22173
6	11	-0.12858	0.19569	-0.12127	-0.05647
6	12	0.04700	-0.03271	0.02773	0.01470
6	13	-0.13390	-0.00309	0.036 72	-0.17762
6	14	-0.02297	0.09231	-0.10085	0.00624
6	15	-0.00697	0.11875	-0.03650	-0.05949
7	1	0.42043	1.76266	1.61781	-0.70011
7	2	-1.73306	-0.44276	-2.84195	0.38552
7	3	1.58631	-0.29854	0.83468	-1.85681
7	4	-0.70798	-0.00683	0.01928	-0.12694
7	5	-0.84105	0.81417	-0.10592	-0.70527
7	6	0.50023	-0.00103	-0.18092	0.91178
7	7	-0.70702	-0.11124	0.19987	-0.58793
7	8	0.16677	0.56344	-0.66850	0.22586
7	9	0.20803	-0.31914	0.35395	0.46763
7	10	0.06335	-0.01063	0.24076	0.11647
7	11	-0.04250	-0.28750	0.24752	-0.11983
7	12	-0.13971	0.28525	-0.19586	0.03015
7	13	0.27651	-0.06010	0.06477	0.17456

Table 4. Rectangular-Harmonic Model Coefficients (con.)

7	14	-0.06703	-0.16502	0.14928	-0.00955
7	15	-0.03639	-0.08032	0.07791	-0.17341
8	1	3.31603	5.58220	-0.44074	-0.79490
8	2	-0.95824	-4.46747	1.86770	-0.39213
8	3	-1.34737	0.91580	-1.44776	0.25701
8	4	1.10121	-0.29209	0.70388	-0.42378
8	5	-0.30687	-0.29736	0.50434	-0.69129
8	6	-0.13969	-0.04296	-0.53447	-0.26891
8	7	-0.03712	0.36213	0.02546	0.62256
8	8	0.25247	-0.45761	0.44310	-0.11620
8	9	-0.34616	0.32148	-0.11331	-0.26649
8	10	0.18843	0.23557	-0.17133	-0.20744
8	11	0.10870	0.05990	-0.11914	0.13291
8	12	-0.02481	-0.19952	0.23894	-0.17592
8	13	-0.19212	0.19060	-0.23797	-0.12452
8	14	0.23414	0.06747	-0.04150	0.19298
8	15	0.01644	-0.09467	-0.00029	0.06760
9	1	-2.18537	3.48995	-1.57473	-4.78597
9	2	2.16019	-2.49957	0.41614	2.09978
9	3	-2.26432	1.03862	0.00126	-1.16616
9	4	0.77841	-0.74632	-0.37452	0.35329

Table 4. Rectangular-Harmonic Model Coefficients (con.)

9	5	-0.17226	0.36005	-0.29210	-0.29683
9	6	0.30127	-0.45394	0.18381	0.83077
9	7	-0.83058	0.26026	0.17586	-0.87825
9	8	0.58998	0.40076	-0.69287	0.66965
9	9	-0.17553	-0.44890	0.51060	-0.08050
9	10	0.04407	0.08372	-0.09538	-0.07233
9	11	0.03944	-0.07694	-0.04026	-0.11101
9	12	0.19002	0.01810	-0.12889	0.32356
9	13	-0.04717	-0.21440	0.33878	-0.09185
9	14	-0.16804	0.06191	-0.16683	-0.13568
9	15	-0.03636	0.08599	-0.00703	0.00700
10	1	-1.53264	0.88371	1.29867	-0.03071
10	2	1.50872	-0.92994	0.03802	-0.20592
10	3	-1.81144	-0.57259	0.06813	-0.74301
10	4	0.16088	0.55026	-0.04285	-0.86953
10	5	-0.30456	-0.23105	0.07705	-0.90593
10	6	0.37293	0.55645	-0.49604	0.22612
10	7	0.07846	-0.58866	0.17024	0.33061
10	8	-0.52099	0.28158	-0.04822	-0.55390
10	9	0.14498	0.07277	-0.16160	0.15475
10	10	-0.02714	0.06984	-0.10329	-0.01712

Table 4. Rectangular-Harmonic Model Coefficients (con.)

10	11	-0.04698	-0.10054	-0.00504	0.13541
10	12	-0.18429	0.17042	-0.07670	-0.12646
10	13	0.25393	0.06462	-0.05330	0.12606
10	14	-0.02404	-0.12619	0.11820	0.00188
10	15	-0.00626	0.00404	-0.00203	-0.00244
11	1	0.68794	2.00314	-1.82657	1.29417
11	2	0.68014	-2.00106	0.49140	-0.01759
11	3	-0.64070	-0.22335	0.41249	-0.07980
11	4	0.40475	0.12301	-0.11870	-0.20360
11	5	-0.43983	-0.53327	-0.08233	-0.20360
11	6	0.04881	0.10360	0.04355	0.38457
11	7	0.13693	0.20792	-0.26172	-0.22968
11	8	0.19715	-0.11042	0.40007	0.01963
11	9	-0.21894	-0.14376	0.01066	0.17168
11	10	-0.08586	0.18476	-0.05054	-0.21125
11	11	0.22761	-0.10226	0.16959	0.12777
11	12	-0.12130	-0.10635	0.08399	0.06518
11	13	0.01405	0.12173	-0.14097	-0.09379
11	14	0.04797	-0.04983	-0.02296	0.06785
11	15	-0.02768	0.07813	-0.00798	-0.01461
12	1	-1.90696	2.52971	-4.09107	3.08946

Table 4. Rectangular-Harmonic Model Coefficients (con.)

12	2	1.59213	-0.73171	1.46118	0.80026
12	3	-0.14431	-0.39781	-0.69909	0.13509
12	4	-0.21148	-0.33016	-0.16375	0.21105
12	5	-0.36754	-0.57927	0.13807	0.37689
12	6	0.33746	0.01655	0.01266	-0.07096
12	7	-0.19403	-0.23841	-0.15226	-0.02569
12	8	-0.20600	0.24767	0.03850	-0.03410
12	9	0.14263	-0.13189	0.02403	0.04626
12	10	-0.15607	0.04710	0.10123	-0.07676
12	11	0.10118	0.10544	-0.21553	0.00513
12	12	-0.01595	-0.14016	0.04774	0.05590
12	13	-0.08750	0.05428	-0.05250	-0.06875
12	14	-0.07930	-0.01179	-0.01840	0.07531
12	15	-0.05007	-0.02926	0.04668	-0.07477
13	1	-4.67324	4.92206	-0.48776	1.65893
13	2	2.04069	-0.47986	-0.02500	-0.68042
13	3	-1.38261	0.21989	-0.59911	0.40972
13	4	0.21093	0.02153	0.64767	0.04682
13	5	-0.49765	0.15527	-0.26342	-0.33375
13	6	0.11866	0.28142	0.20178	0.04789
13	7	-0.12871	-0.11888	-0.28160	-0.11622

Table 4. Rectangular-Harmonic Model Coefficients (con.)

13	8	0.07702	0.09139	-0.03837	0.21612
13	9	-0.02636	-0.06746	-0.03337	-0.16914
13	10	0.10606	0.11825	0.03435	0.12884
13	11	-0.01994	-0.11033	0.06455	-0.12492
13	12	-0.08246	0.07670	-0.05334	0.12445
13	13	0.05388	0.01529	0.06806	-0.03654
13	14	-0.03364	-0.03445	-0.08154	0.04046
13	15	-0.00051	-0.02318	0.07854	0.00493
14	1	-2.14450	5.23947	2.84025	-1.75222
14	2	2.05113	-1.83951	-1.14319	-0.07571
14	3	-1.51667	-0.12111	1.02495	0.36313
14	4	0.75293	0.22577	0.05374	-0.51673
14	5	-0.49578	-0.32312	-0.04813	0.14631
14	6	0.37889	0.15998	0.29040	-0.16016
14	7	-0.34865	-0.31172	-0.06350	-0.06328
14	8	-0.05944	0.34002	-0.07941	0.01225
14	9	0.10337	-0.23342	0.11621	0.03923
14	10	-0.15907	0.09641	-0.12157	-0.24132
14	11	0.09470	0.00729	-0.07918	0.15628
14	12	-0.06836	0.00526	0.13284	-0.10855
14	13	0.02588	0.04462	-0.14339	-0.02591

Table 4. Rectangular-Harmonic Model Coefficients (con.)

14	14	0.00271	0.00534	0.06132	0.10086
14	15	0.01955	-0.01534	0.02426	-0.01894
15	1	-0.49015	1.55673	2.55386	-5.02614
15	2	0.11961	-0.83393	-2.46010	0.95284
15	3	-0.15853	0.47131	1.06937	0.71696
15	4	0.38033	-0.33976	-0.27622	-0.51193
15	5	-0.51728	-0.04921	-0.04423	0.35401
15	6	0.34257	0.22986	-0.06258	0.05729
15	7	-0.01659	-0.26012	0.16216	0.07511
15	8	-0.17459	0.09203	0.07409	-0.04397
15	9	0.11633	0.02952	-0.03338	0.05132
15	10	-0.06943	-0.10939	0.08129	0.00419
15	11	0.05010	-0.10604	0.00194	-0.01563
15	12	0.06284	-0.10455	0.05631	0.01565
15	13	-0.11932	0.00911	0.00218	-0.07397
15	14	0.04238	0.04580	-0.04159	0.00744
15	15	-0.01570	-0.01475	0.00892	-0.00096

$$B_z(\theta,\varphi,-H) = \sum_{\nu=-N}^{N} \sum_{\mu=-M}^{M} b_{z\nu\mu}(-H)\, e^{i(\nu\theta+\mu\varphi)} \tag{25c}$$

The complex-valued Fourier coefficients $b_{x\,\mu\,\nu}(-H)$, $b_{y\,\mu\,\nu}(-H)$, and $b_{z\,\mu\,\nu}(-H)$, which have units of nanoTeslas (nT), are known quantities since they can be obtained by taking the FFT of their respective X-, Y- or Z-component, magnetic-residual, survey-generated grids. Consequently, when eqs. (25a, 25b, and 25c) are inserted into eqs. (22a through 22d, 23a through 23d, and 24a through 24d), the rectangular-harmonic coefficients can be analytically evaluated in terms of their respective Fourier coefficients by converting the sine and cosine functions in the above expressions to their exponential forms and employing the Dirac delta function identity:

$$\int_{-\pi}^{\pi} e^{i(\lambda-\lambda')\eta}\, d\eta = 2\pi\,\delta(\lambda-\lambda') \tag{26}$$

over all integrals involving the parameters θ and φ. The integrals to be evaluated are of just the following two basic forms:

$$\int_{-\pi}^{\pi} e^{-i\lambda\Omega} \sin\kappa\Omega\, d\Omega = i\pi\,\delta(\kappa+\lambda) - i\pi\,\delta(\kappa-\lambda) \tag{27a}$$

$$\int_{-\pi}^{\pi} e^{-i\lambda\Omega} \cos\kappa\Omega\, d\Omega = \pi\,\delta(\kappa+\lambda) + \pi\,\delta(\kappa-\lambda) \tag{27b}$$

Consequently, eqs. (22a) through (22d) are evaluated as:

$$A_{nm} = + \frac{iL_x}{nL}\left(b_{x,-n,-m} - b_{x,n,-m} + b_{x,-n,m} - b_{x,n,m}\right)e^{k_{nm}H} \tag{28a}$$

$$B_{nm} = + \frac{L_x}{nL}\left(b_{x,-n,-m} - b_{x,n,-m} - b_{x,-n,m} + b_{x,nm}\right)e^{k_{nm}H} \tag{28b}$$

$$D_{nm} = + \frac{L_x}{nL}\left(b_{x,-n,-m} + b_{x,n,-m} + b_{x,-n,m} + b_{x,nm}\right)e^{k_{nm}H} \tag{28c}$$

$$E_{nm} = - \frac{iL_x}{nL}\left(b_{x,-n,-m} + b_{x,n,-m} - b_{x,-n,m} - b_{x,nm}\right)e^{k_{nm}H} \tag{28d}$$

Equations (23a) through (23d) become:

$$A_{nm} = + \frac{iL_y}{mL}\left(b_{y,-n,-m} + b_{y,n,-m} - b_{y,-n,m} - b_{y,n,m}\right)e^{k_{nm}H} \tag{29a}$$

$$B_{nm} = + \frac{L_y}{mL}\left(b_{y,-n,-m} + b_{y,n,-m} + b_{y,-n,m} + b_{y,n,m}\right)e^{k_{nm}H} \tag{29b}$$

$$D_{nm} = + \frac{L_y}{mL}\left(b_{y,-n,-m} - b_{y,n,-m} - b_{y,-n,m} + b_{y,n,m}\right)e^{k_{nm}H} \tag{29c}$$

$$E_{nm} = - \frac{iL_y}{mL}\left(b_{y,-n,-m} - b_{y,n,-m} + b_{y,-n,m} - b_{y,n,m}\right)e^{k_{nm}H} \tag{29d}$$

The evaluation of eqs. (24a) through (24d) yields the third alternative means of computing the rectangular-harmonic, magnetic-potential coefficients:

$$A_{nm} = - \frac{2\pi}{k_{nm}L}\left(b_{z,-n,-m} + b_{z,n,-m} + b_{z,-n,m} + b_{z,n,m}\right)e^{k_{nm}H} \tag{30a}$$

$$B_{nm} = + \frac{2\pi i}{k_{nm}L}\left(b_{z,-n,-m} + b_{z,n,-m} - b_{z,-n,m} - b_{z,nm}\right)e^{k_{nm}H} \tag{30b}$$

$$D_{nm} = + \frac{2\pi i}{k_{nm} L} \left(b_{z,-n,-m} - b_{z,n,-m} + b_{z,-n,m} - b_{z,n,m} \right) e^{k_{nm} H} \qquad (30c)$$

$$E_{nm} = + \frac{2\pi}{k_{nm} L} \left(b_{z,-n,-m} - b_{z,n,-m} - b_{z,-n,m} + b_{z,n,m} \right) e^{k_{nm} H} \qquad (30d)$$

The rectangular-harmonic coefficients of the local magnetic potential are thus determined through a two-step process:

(1) Perform an FFT on one of the three available gridded vector components of the local magnetic field.

(2) Use the Fourier coefficients obtained in step 1 to evaluate the rectangular-harmonic coefficients of the local magnetic potential using the corresponding set of equations derived above for these coefficients.

3.2.1 Computing the Local Magnetic-Field Vector from the Model

Having evaluated the coefficients of the local rectangular-harmonic model, it is now desirable to recompute all three vector-magnetic components B_x , B_y , and B_z . The reason for this is that the grids derived from the survey data are not entirely consistent with each other because of instrument noise and other experimental factors. However, the magnetic-field components derived from the model are necessarily consistent with each other by definition. As a consequence, geophysical interpretations of a region based on least-squares or other inverse-modeling techniques, using magnetic-field parameters derived in this way, are less ambiguous due to the reduced noise level of the inverted data. Secondly, it is sometimes desirable to upward or downward continue the original survey data to some other altitude H'. A

local potential-field model permits this procedure to be performed with relative ease using FFT procedures and specially designed filters, if they are needed.

We now assume that the rectangular-harmonic coefficients, A_{nm}, B_{nm}, D_{nm}, and E_{nm} are known and seek to determine their corresponding Fourier coefficients $b_{x\nu\mu}(-H')$, $b_{y\nu\mu}(-H')$, and $b_{z\nu\mu}(-H')$. Equations (25a, 25b, and 25c) can easily be inverted via the usual techniques, which involve the use of eq. (26) to yield:

$$b_{x\nu\mu}(-H') = (4\pi^2)^{-1} \int_{-\pi}^{\pi}\int_{-\pi}^{\pi} e^{-i(\nu\theta+\mu\varphi)} B_x(\theta,\varphi,-H')\,d\theta\,d\varphi \tag{31a}$$

$$b_{y\nu\mu}(-H') = (4\pi^2)^{-1} \int_{-\pi}^{\pi}\int_{-\pi}^{\pi} e^{-i(\nu\theta+\mu\varphi)} B_y(\theta,\varphi,-H')\,d\theta\,d\varphi \tag{31b}$$

$$b_{z\nu\mu}(-H') = (4\pi^2)^{-1} \int_{-\pi}^{\pi}\int_{-\pi}^{\pi} e^{-i(\nu\theta+\mu\varphi)} B_z(\theta,\varphi,-H')\,d\theta\,d\varphi \tag{31c}$$

where we temporarily drop the tensor notation and explicitly reference parameters related to the magnetic-vector components by the subscripts x, y, and z, while parameters related to the magnetic-gradient components will be explicitly referenced by the subscripts xx, xy, xz, yz, etc. Greek letters will then be used to reference either Fourier coefficients or rectangular-harmonic coefficients with the understanding that rectangular-harmonic coefficients with indices equal to or less than zero are defined to be zero. Greek indices now have the ranges: $-N \le \nu \le +N$ and $-M \le \mu \le +M$, where for the Juan de Fuca/Explorer plate region $N = M = 128$.

After inserting eqs. (21a, 21b, and 21c) into eqs. (31a, 31b, and 31c), respectively, and performing the necessary integrations, which are of the following three basic forms:

$$\int_{-\pi}^{\pi}\int_{-\pi}^{\pi} e^{-i(\nu\xi+\mu\eta)} \cos j\xi \cos k\eta \, d\xi \, d\eta = \pi^2 \{\delta(j-\nu)\delta(k-\mu) + \delta[(-j)-\nu]\delta(k-\mu) + \delta(j-\nu)\delta[(-k)-\mu] + \delta[(-j)-\nu]\delta[(-k)-\mu]\} \tag{32a}$$

$$\int_{-\pi}^{\pi}\int_{-\pi}^{\pi} e^{-i(\nu\xi+\mu\eta)} \cos j\xi \sin k\eta \, d\xi \, d\eta = -i\pi^2 \{\delta(j-\nu)\delta(k-\mu) + \delta[(-j)-\nu]\delta(k-\mu) - \delta(j-\nu)\delta[(-k)-\mu] - \delta[(-j)-\nu]\delta[(-k)-\mu]\} \tag{32b}$$

$$\int_{-\pi}^{\pi}\int_{-\pi}^{\pi} e^{-i(\nu\xi+\mu\eta)} \sin j\xi \sin k\eta \, d\xi \, d\eta = -\pi^2 \{\delta(j-\nu)\delta(k-\mu) - \delta[(-j)-\nu]\delta(k-\mu) - \delta(j-\nu)\delta[(-k)-\mu] - \delta[(-j)-\nu]\delta[(-k)-\mu]\} \tag{32c}$$

where again the Dirac Delta function identity of eq. (26) has been used, we obtain with minimal effort the following results:

$$b_{x\nu\mu}(-H') = +\frac{\nu L}{4L_x}\left[i\left(A_{\nu,\mu} + A_{-\nu,\mu} + A_{\nu,-\mu} + A_{-\nu,-\mu}\right) + \left(B_{\nu,\mu} + B_{-\nu,\mu} - B_{\nu,-\mu} - B_{-\nu,-\mu}\right) - \left(D_{\nu,\mu} + D_{-\nu,\mu} + D_{\nu,-\mu} + D_{-\nu,-\mu}\right) + i\left(E_{\nu,\mu} - E_{-\nu,\mu} - E_{\nu,-\mu} + E_{-\nu,-\mu}\right)\right] e^{-k_{\nu\mu}H'} \tag{33a}$$

$$b_{y\nu\mu}(-H') = +\frac{\mu L}{4L_y}\left[i\left(A_{\nu,\mu} + A_{-\nu,\mu} + A_{\nu,-\mu} + A_{-\nu,-\mu}\right) - \left(B_{\nu,\mu} + B_{-\nu,\mu} - B_{\nu,-\mu} - B_{-\nu,-\mu}\right) + \left(D_{\nu,\mu} - D_{-\nu,\mu} + D_{\nu,-\mu} - D_{-\nu,-\mu}\right) + i\left(E_{\nu,\mu} - E_{-\nu,\mu} - E_{\nu,-\mu} + E_{-\nu,-\mu}\right)\right] e^{-k_{\nu\mu}H'} \tag{33b}$$

$$b_{z\nu\mu}(-H') = +\frac{k_{\nu\mu}L}{8\pi}\left[\left(A_{\nu,\mu} + A_{-\nu,\mu} + A_{\nu,-\mu} + A_{-\nu,-\mu}\right) - i\left(B_{\nu,\mu} + B_{-\nu,\mu} - B_{\nu,-\mu} - B_{-\nu,-\mu}\right) - i\left(D_{\nu,\mu} - D_{-\nu,\mu} + D_{\nu,-\mu} - D_{-\nu,-\mu}\right) - \left(E_{\nu,\mu} - E_{-\nu,\mu} - E_{\nu,-\mu} + E_{-\nu,-\mu}\right)\right] e^{-k_{\nu\mu}H'} \tag{33c}$$

where it is understood that the rectangular-harmonic coefficients are defined to be zero if any index is less than or equal to zero. The above result was obtained using the fact that $k_{\nu,\mu} = k_{-\nu,\mu} = k_{\nu,-\mu} = k_{-\nu,-\mu}$.

Having thus determined the Fourier coefficients from the model, an application of the Inverse FFT, which is essentially an application of eqs. (25a, 25b, and 25c) with H replaced by H' (the new upward/downward continued altitude), yields the desired self-consistent set of uniformly spaced grids for the local magnetic-field vector components. For the Juan de Fuca/Explorer region, these are illustrated in Figures 3a , 3b , and 3c , corresponding to the X-, Y-, and Z-components at the original survey altitude H' = H.

3.2.2 Computing the Magnetic-Gradient Tensor from the Model

The magnetic-gradient tensor $\mathscr{B}(x,y,z)$ is the gradient of the magnetic field $\mathbf{B}(x,y,z)$. That is:

$$\mathscr{B}(x,y,z) = \nabla \mathbf{B}(x,y,z) \tag{34}$$

In tensor notation, this equation becomes:

$$\mathscr{B}_{\mu\nu}(x,y,z) = B_{\mu/\nu}(x,y,z) = -V_{/\mu/\nu}(x,y,z) \tag{35}$$

Since interchanging the order of differentiation of the magnetic potential does not affect the result, the magnetic-gradient tensor is necessarily symmetric. The local magnetic potential also must satisfy Laplace's equation. This is equivalent to stating that the trace of the magnetic-gradient tensor must be zero. Contracting the indices μ and ν yields the trace:

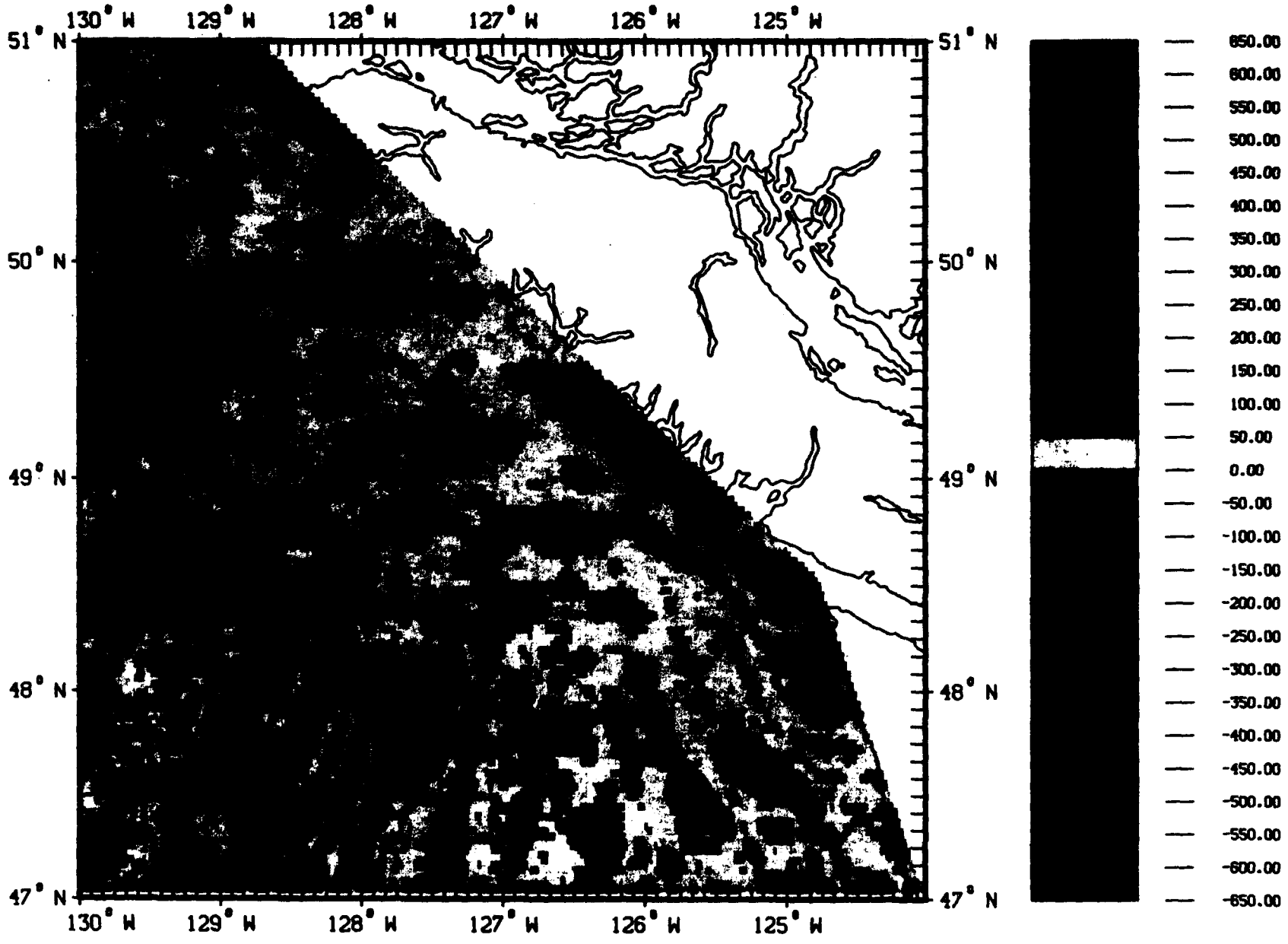

Figure 3a. Juan de Fuca X-Component Magnetic Field; Units: nT

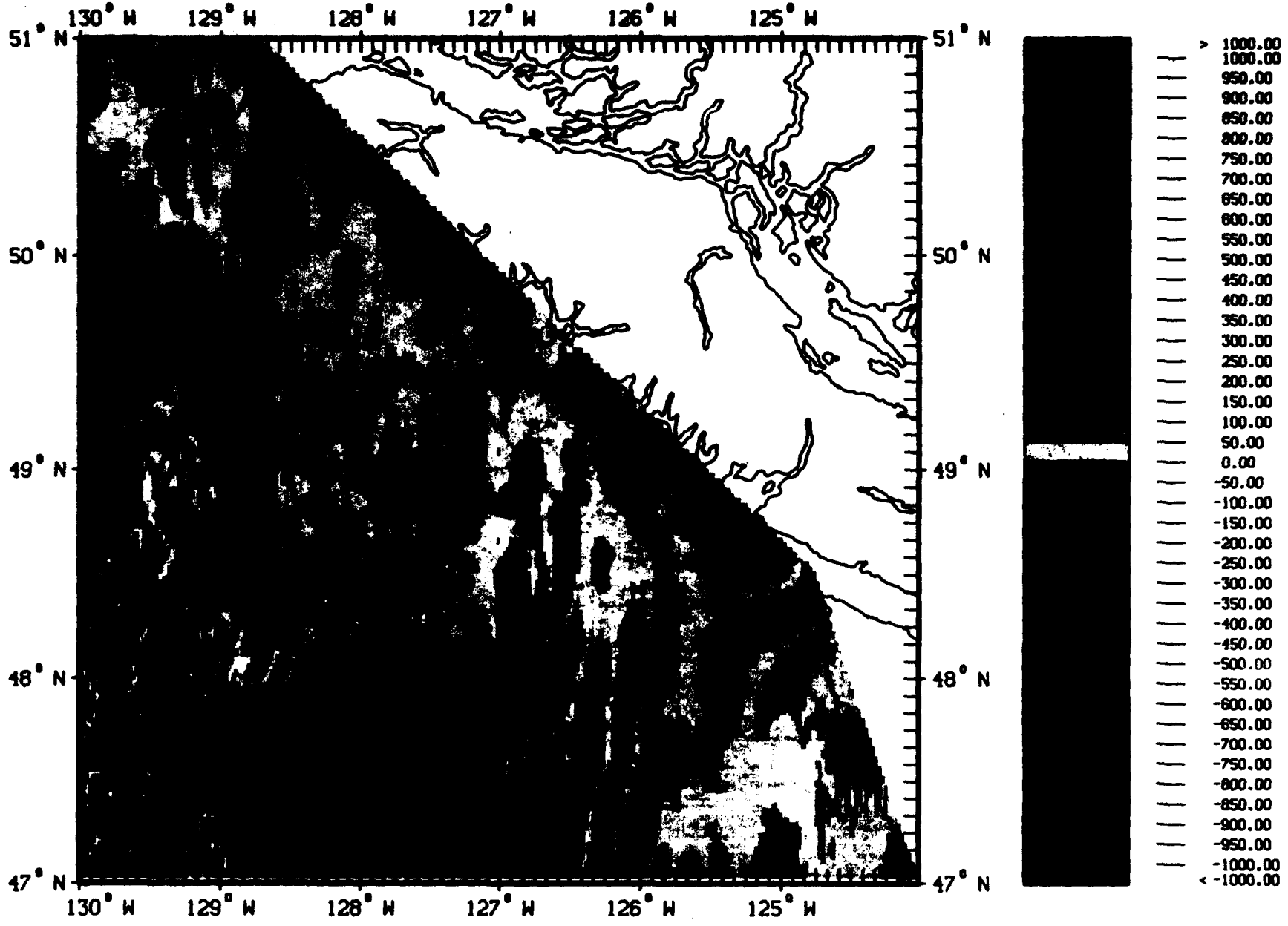

Figure 3b. Juan de Fuca Y-Component Magnetic Field; Units: nT

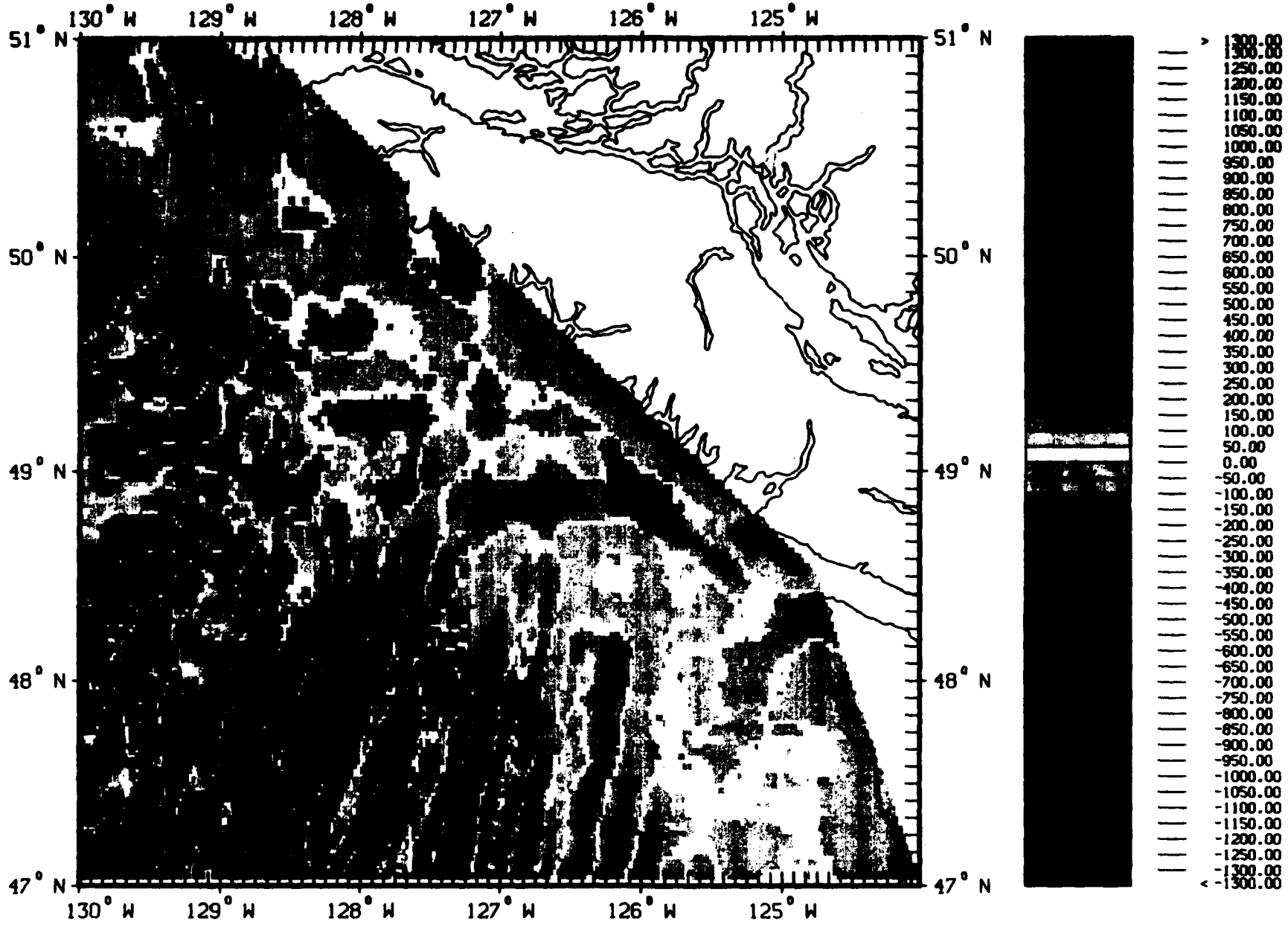

Figure 3c. Juan de Fuca Z-Component Magnetic Field; Units: nT

$$\mathcal{B}^{n}_{\mu} = 0 \tag{36}$$

The symmetry and trace conditions on the local magnetic gradient $\mathcal{B}(x,y,z)$ reduce the number of its independent components to five from the original nine, just as was the case with the regional magnetic gradient. Of the five independent components, two must be diagonal elements, and three must be off-diagonal elements. We will nevertheless examine all three diagonal components as well as three off-diagonal components for a total of six components. Then, taking the indicated derivatives of the local magnetic potential, the five independent components plus one extra diagonal component take the following forms:

$$\mathcal{B}_{xx}(x,y,z) = -\frac{2\pi L}{L_x^2}\sum_{n=1}^{N}\sum_{m=1}^{M} n^2\left[A_{nm}\cos n\theta(x)\cos m\varphi(y) + B_{nm}\cos n\theta(x)\sin m\varphi(y) + D_{nm}\sin n\theta(x)\cos m\varphi(y) + E_{nm}\sin n\theta(x)\sin m\varphi(y)\right]e^{k_{nm}z} \tag{37a}$$

$$\mathcal{B}_{xy}(x,y,z) = +\frac{2\pi}{L}\sum_{n=1}^{N}\sum_{m=1}^{M} nm\left[A_{nm}\sin n\theta(x)\sin m\varphi(y) - B_{nm}\sin n\theta(x)\cos m\varphi(y) - D_{nm}\cos n\theta(x)\sin m\varphi(y) + E_{nm}\cos n\theta(x)\cos m\varphi(y)\right]e^{k_{nm}z} \tag{37b}$$

$$\mathcal{B}_{xz}(x,y,z) = -\frac{L}{L_x}\sum_{n=1}^{N}\sum_{m=1}^{M} n k_{nm}\left[A_{nm}\sin n\theta(x)\cos m\varphi(y) + B_{nm}\sin n\theta(x)\sin m\varphi(y) - D_{nm}\cos n\theta(x)\cos m\varphi(y) - E_{nm}\cos n\theta(x)\sin m\varphi(y)\right]e^{k_{nm}z} \tag{37c}$$

$$\mathcal{B}_{yy}(x,y,z) = -\frac{2\pi L}{L_y^2}\sum_{n=1}^{N}\sum_{m=1}^{M} m^2\left[A_{nm}\cos n\theta(x)\cos m\varphi(y) + B_{nm}\cos n\theta(x)\sin m\varphi(y) + D_{nm}\sin n\theta(x)\cos m\varphi(y) + E_{nm}\sin n\theta(x)\sin m\varphi(y)\right]e^{k_{nm}z} \tag{37d}$$

$$\mathcal{B}_{yz}(x,y,z) = -\frac{L}{L_y}\sum_{n=1}^{N}\sum_{m=1}^{M} m k_{nm}\left[A_{nm}\cos n\theta(x)\sin m\varphi(y) - B_{nm}\cos n\theta(x)\cos m\varphi(y) + D_{nm}\sin n\theta(x)\sin m\varphi(y) - E_{nm}\sin n\theta(x)\cos m\varphi(y)\right]e^{k_{nm}z} \quad (37e)$$

$$\mathcal{B}_{zz}(x,y,z) = +\frac{L}{2\pi}\sum_{n=1}^{N}\sum_{m=1}^{M} k_{nm}^2\left[A_{nm}\cos n\theta(x)\cos m\varphi(y) + B_{nm}\cos m\theta(x)\sin m\varphi(y) + D_{nm}\sin n\theta(x)\cos m\varphi(y) + E_{nm}\sin n\theta(x)\sin m\varphi(y)\right]e^{k_{nm}z} \quad (37f)$$

On the other hand, each of the magnetic-gradient components may be written in the form of a 2-dimensional finite Fourier Transform at an altitude z = -H' which may possibly be upward/downward continued from the survey altitude z_s = -H , so that:

$$\mathcal{B}_{xx}(\theta,\varphi,-H') = \sum_{\nu=-N}^{N}\sum_{\mu=-M}^{M}\beta_{xx\nu\mu}(-H')\,e^{i(\nu\theta+\mu\varphi)} \quad (38a)$$

$$\mathcal{B}_{xy}(\theta,\varphi,-H') = \sum_{\nu=-N}^{N}\sum_{\mu=-M}^{M}\beta_{xy\nu\mu}(-H')\,e^{i(\nu\theta+\mu\varphi)} \quad (38b)$$

$$\mathcal{B}_{xz}(\theta,\varphi,-H') = \sum_{\nu=-N}^{N}\sum_{\mu=-M}^{M}\beta_{xz\nu\mu}(-H')\,e^{i(\nu\theta+\mu\varphi)} \quad (38c)$$

$$\mathcal{B}_{yy}(\theta,\varphi,-H') = \sum_{\nu=-N}^{N}\sum_{\mu=-M}^{M}\beta_{yy\nu\mu}(-H')\,e^{i(\nu\theta+\mu\varphi)} \quad (38d)$$

$$\mathcal{B}_{yz}(\theta,\varphi,-H') = \sum_{\nu=-N}^{N}\sum_{\mu=-M}^{M}\beta_{yz\nu\mu}(-H')\,e^{i(\nu\theta+\mu\varphi)} \quad (38e)$$

$$\mathscr{B}_{zz}(\theta,\varphi,-H') = \sum_{\nu=-N}^{N}\sum_{\mu=-M}^{M} \beta_{zz\nu\mu}(-H')\, e^{i(\nu\theta+\mu\varphi)} \tag{38f}$$

Using eq. (26), eqs. (37a through 37f) can be inverted to yield the Fourier coefficients in terms of the rectangular-harmonic coefficients A_{mn}, B_{mn}, D_{mn}, and E_{mn} yielding:

$$\beta_{xx\nu\mu}(-H') = (4\pi^2)^{-1} \int_{-\pi}^{\pi}\int_{-\pi}^{\pi} e^{-i(\nu\theta+\mu\varphi)}\, \mathscr{B}_{xx}(\theta,\varphi,-H')\, d\theta\, d\varphi \tag{39a}$$

$$\beta_{xy\nu\mu}(-H') = (4\pi^2)^{-1} \int_{-\pi}^{\pi}\int_{-\pi}^{\pi} e^{-i(\nu\theta+\mu\varphi)}\, \mathscr{B}_{xy}(\theta,\varphi,-H')\, d\theta\, d\varphi \tag{39b}$$

$$\beta_{xz\nu\mu}(-H') = (4\pi^2)^{-1} \int_{-\pi}^{\pi}\int_{-\pi}^{\pi} e^{-i(\nu\theta+\mu\varphi)}\, \mathscr{B}_{xz}(\theta,\varphi,-H')\, d\theta\, d\varphi \tag{39c}$$

$$\beta_{yy\nu\mu}(-H') = (4\pi^2)^{-1} \int_{-\pi}^{\pi}\int_{-\pi}^{\pi} e^{-i(\nu\theta+\mu\varphi)}\, \mathscr{B}_{yy}(\theta,\varphi,-H')\, d\theta\, d\varphi \tag{39d}$$

$$\beta_{yz\nu\mu}(-H') = (4\pi^2)^{-1} \int_{-\pi}^{\pi}\int_{-\pi}^{\pi} e^{-i(\nu\theta+\mu\varphi)}\, \mathscr{B}_{yz}(\theta,\varphi,-H')\, d\theta\, d\varphi \tag{39e}$$

$$\beta_{zz\nu\mu}(-H') = (4\pi^2)^{-1} \int_{-\pi}^{\pi}\int_{-\pi}^{\pi} e^{-i(\nu\theta+\mu\varphi)}\, \mathscr{B}_{zz}(\theta,\varphi,-H')\, d\theta\, d\varphi \tag{39f}$$

Inserting eqs. (36a through 36f) into eqs. (38a through 38f), respectively, and using eqs. (27a and 27b) to evaluate the resulting integrals, the Fourier coefficients for the magnetic gradient components reduce in a straightforward manner to the following:

$$\beta_{xx\nu\mu}(-H') = -\frac{2\pi^3 L}{L_x^2}\nu^2\Big[\Big(A_{\nu,\mu} + A_{-\nu,\mu} + A_{\nu,-\mu} + A_{-\nu,-\mu}\Big)$$
$$-i\Big(B_{\nu,\mu} + B_{-\nu,\mu} - B_{\nu,-\mu} - B_{-\nu,-\mu}\Big)$$
$$-i\Big(D_{\nu,\mu} - D_{-\nu,\mu} + D_{\nu,-\mu} - D_{-\nu,-\mu}\Big)$$
$$-\Big(E_{\nu,\mu} - E_{-\nu,\mu} - E_{\nu,-\mu} + E_{-\nu,-\mu}\Big)\Big]e^{-k_{\nu\mu}H'} \qquad (40a)$$

$$\beta_{xy\nu\mu}(-H') = -\frac{2\pi^3}{L}\nu\mu\Big(A_{\nu,\mu} + A_{-\nu,\mu} + A_{\nu,-\mu} + A_{-\nu,-\mu}\Big)$$
$$-i\Big(B_{\nu,\mu} + B_{-\nu,\mu} - B_{\nu,-\mu} - B_{-\nu,-\mu}\Big)$$
$$-i\Big(D_{\nu,\mu} - D_{-\nu,\mu} + D_{\nu,-\mu} - D_{-\nu,-\mu}\Big)$$
$$-\Big(E_{\nu,\mu} - E_{-\nu,\mu} - E_{\nu,-\mu} + E_{-\nu,-\mu}\Big)\Big]e^{-k_{\nu\mu}H'} \qquad (40b)$$

$$\beta_{xz\nu\mu}(-H') = +\frac{\pi^2 L}{L_x}\nu k_{\nu\mu}\Big[i\Big(A_{\nu,\mu} + A_{-\nu,\mu} + A_{\nu,-\mu} + A_{-\nu,-\mu}\Big)$$
$$+\Big(B_{\nu,\mu} + B_{-\nu,\mu} - B_{\nu,-\mu} - B_{-\nu,-\mu}\Big)$$
$$+\Big(D_{\nu,\mu} - D_{-\nu,\mu} + D_{\nu,-\mu} - D_{-\nu,-\mu}\Big)$$
$$-i\Big(E_{\nu,\mu} - E_{-\nu,\mu} - E_{\nu,-\mu} + E_{-\nu,-\mu}\Big)\Big]e^{-k_{\nu\mu}H'} \qquad (40c)$$

$$\beta_{yy\nu\mu}(-H') = -\frac{2\pi^3 L}{L_y^2}\mu^2\Big[\Big(A_{\nu,\mu} + A_{-\nu,\mu} + A_{\nu,-\mu} + A_{-\nu,-\mu}\Big)$$
$$-i\Big(B_{\nu,\mu} + B_{-\nu,\mu} - B_{\nu,-\mu} - B_{-\nu,-\mu}\Big)$$
$$-i\Big(D_{\nu,\mu} - D_{-\nu,\mu} + D_{\nu,-\mu} - D_{-\nu,-\mu}\Big)$$
$$-\Big(E_{\nu,\mu} - E_{-\nu,\mu} - E_{\nu,-\mu} + E_{-\nu,-\mu}\Big)\Big]e^{-k_{\nu\mu}H'} \qquad (40d)$$

$$\beta_{yzv\mu}(-H') = + \frac{\pi^2 L}{L_y} \mu k_{v\mu} \Big[i\Big(A_{v,\mu} + A_{-v,\mu} + A_{v,-\mu} + A_{-v,-\mu}\Big) + \Big(B_{v,\mu} + B_{-v,\mu} - B_{v,-\mu} - B_{-v,-\mu}\Big) + \Big(D_{v,\mu} - D_{-v,\mu} + D_{v,-\mu} - D_{-v,-\mu}\Big) - i\Big(E_{v,\mu} - E_{-v,\mu} - E_{v,-\mu} + E_{-v,-\mu}\Big)\Big] e^{-k_{v\mu}H'} \tag{40e}$$

$$\beta_{zzv\mu}(-H') = + \frac{\pi L}{2} k_{v\mu}^2 \Big[\Big(A_{v,\mu} + A_{-v,\mu} + A_{v,-\mu} + A_{-v,-\mu}\Big) - i\Big(B_{v,\mu} + B_{-v,\mu} - B_{v,-\mu} - B_{-v,-\mu}\Big) - i\Big(D_{v,\mu} - D_{-v,\mu} + D_{v,-\mu} - D_{-v,-\mu}\Big) - \Big(E_{v,\mu} - E_{-v,\mu} - E_{v,-\mu} + E_{-v,-\mu}\Big)\Big] e^{-k_{v\mu}H'} \tag{40f}$$

Thus, given that the rectangular-harmonic coefficients have previously been determined as explained in section 3.2, the Fourier coefficients, which are associated with the local rectangular-harmonic potential, are easily computed through eqs. (40a through 40f) and then inserted into eqs. (38a through 38f), which may be used in conjunction with an FFT algorithm to generate all of the local magnetic-gradient components of the surveyed area. Figures 4a through 4f illustrate the result of this computational process for 6 local magnetic-gradient components of the Northern Juan de Fuca/Explorer plate region. Figures 4a through 4f correspond to the magnetic gradients $\mathcal{B}_{xx}$, $\mathcal{B}_{xy}$, $\mathcal{B}_{xz}$, $\mathcal{B}_{yy}$, $\mathcal{B}_{yz}$, and $\mathcal{B}_{zz}$, respectively. Figure 4f in particular clearly displays the north-south oriented, magnetic-reversal lineation patterns of the Juan de Fuca ridge axis and the magnetically quiet subduction zone adjacent to the axis.

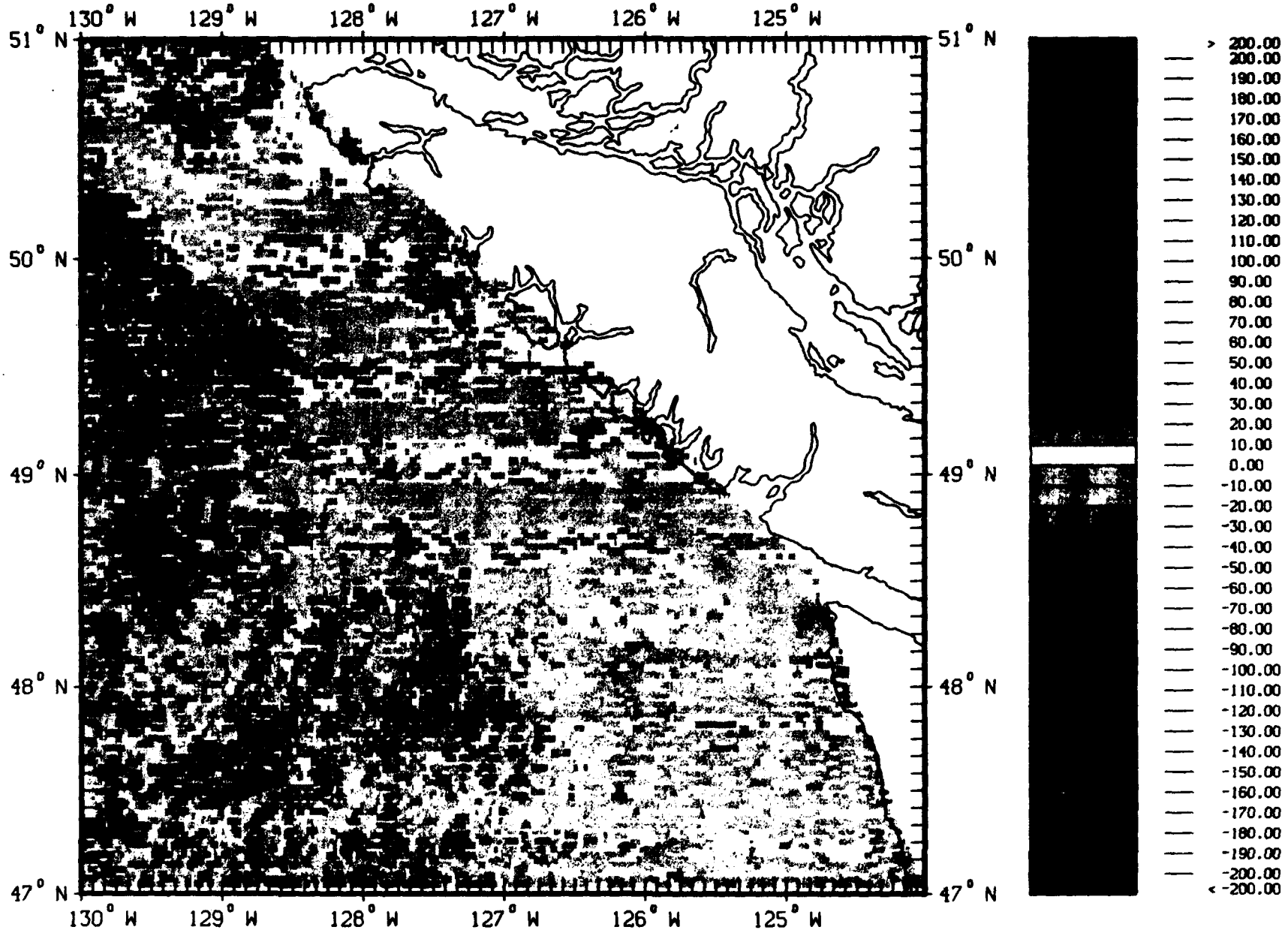

Figure 4a. Juan de Fuca XX-Component Magnetic-Field Gradient; Units: nT/km

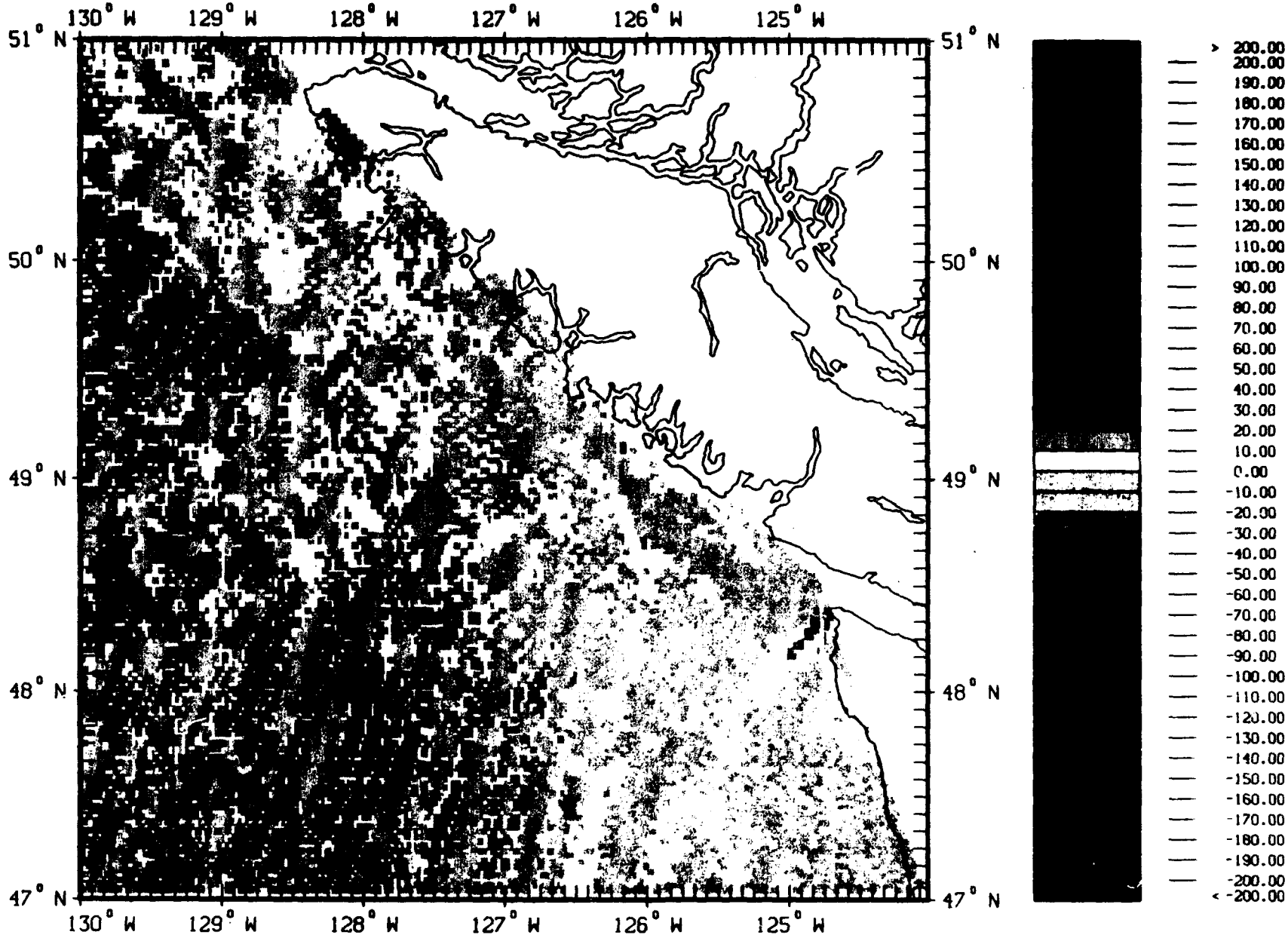

Figure 4b. Juan de Fuca XY-Component Magnetic-Field Gradient; Units: nT/km

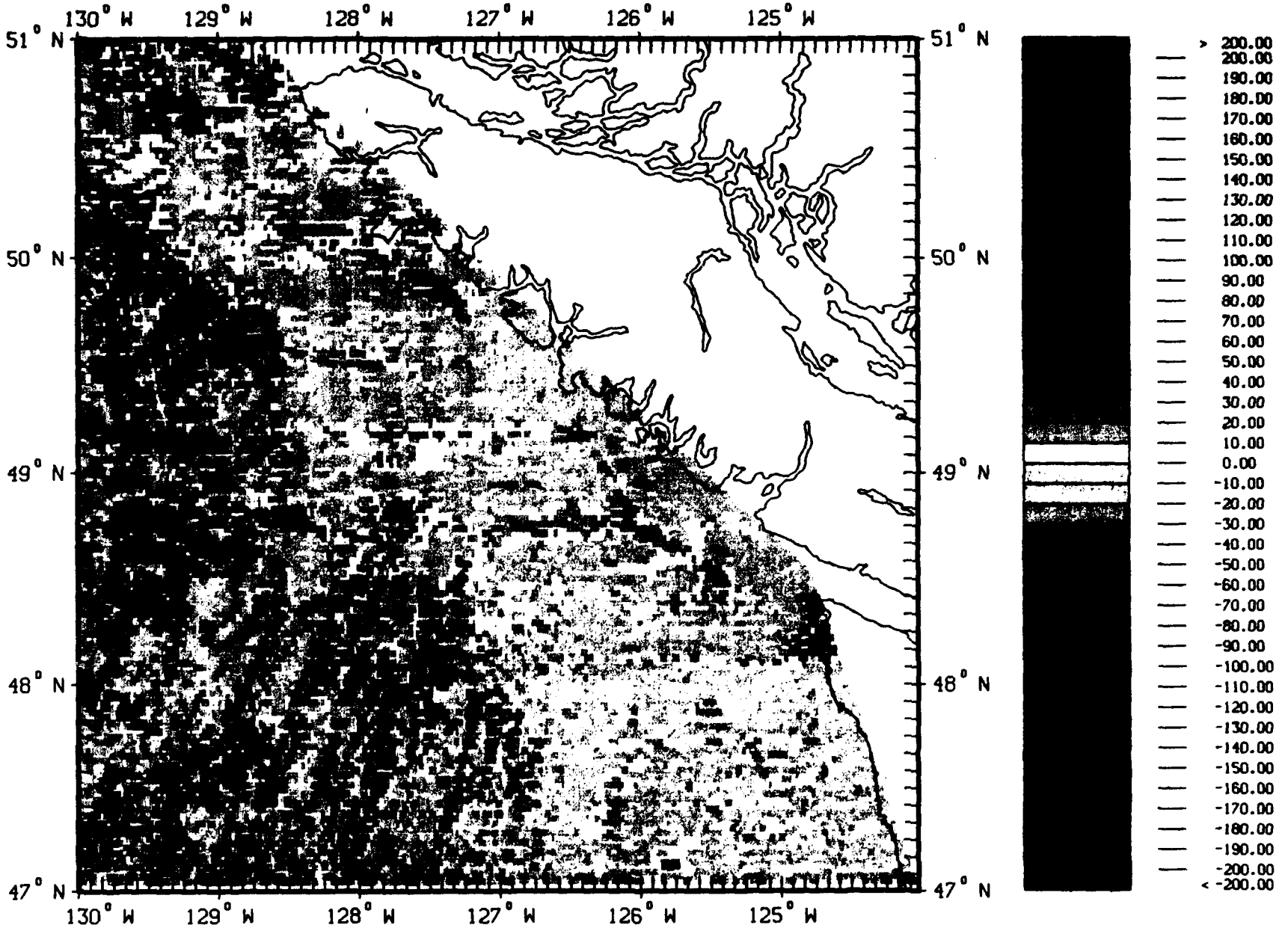

Figure 4c. Juan de Fuca XZ-Component Magnetic-Field Gradient; Units: nT/km

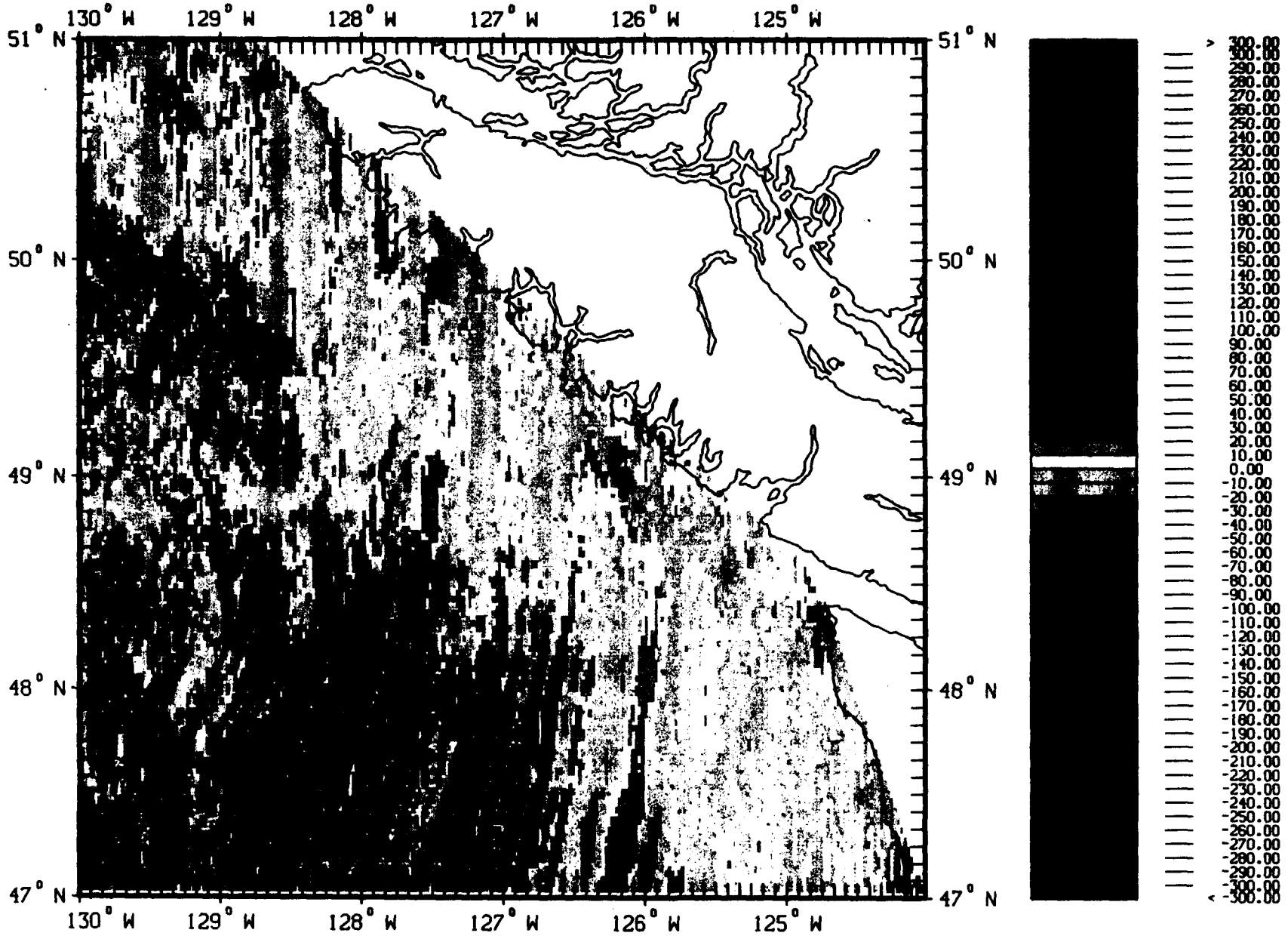

Figure 4d. Juan de Fuca YY-Component Magnetic-Field Gradient; Units: nT/km

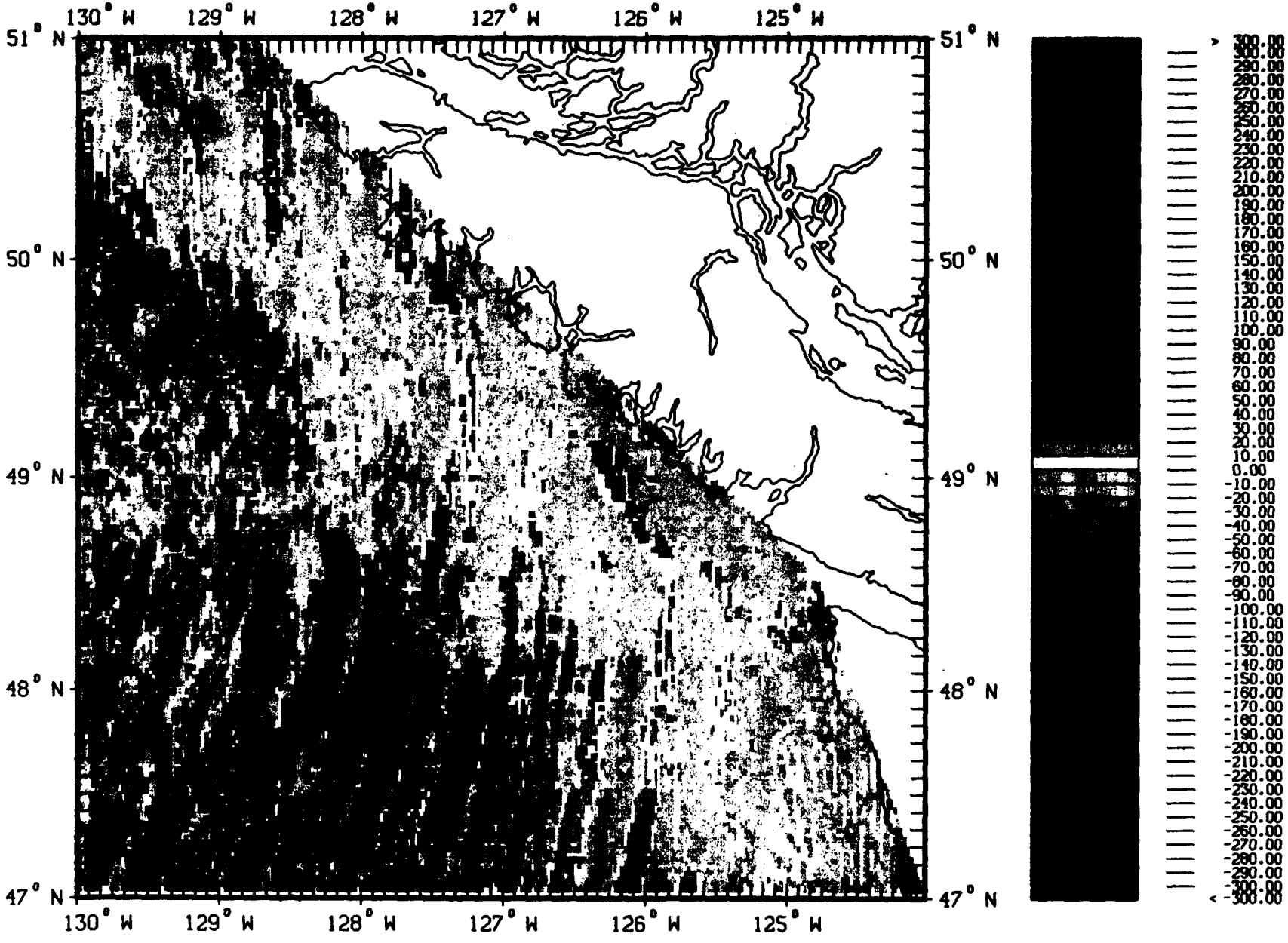

Figure 4e. Juan de Fuca YZ-Component Magnetic-Field Gradient; Units: nT/km

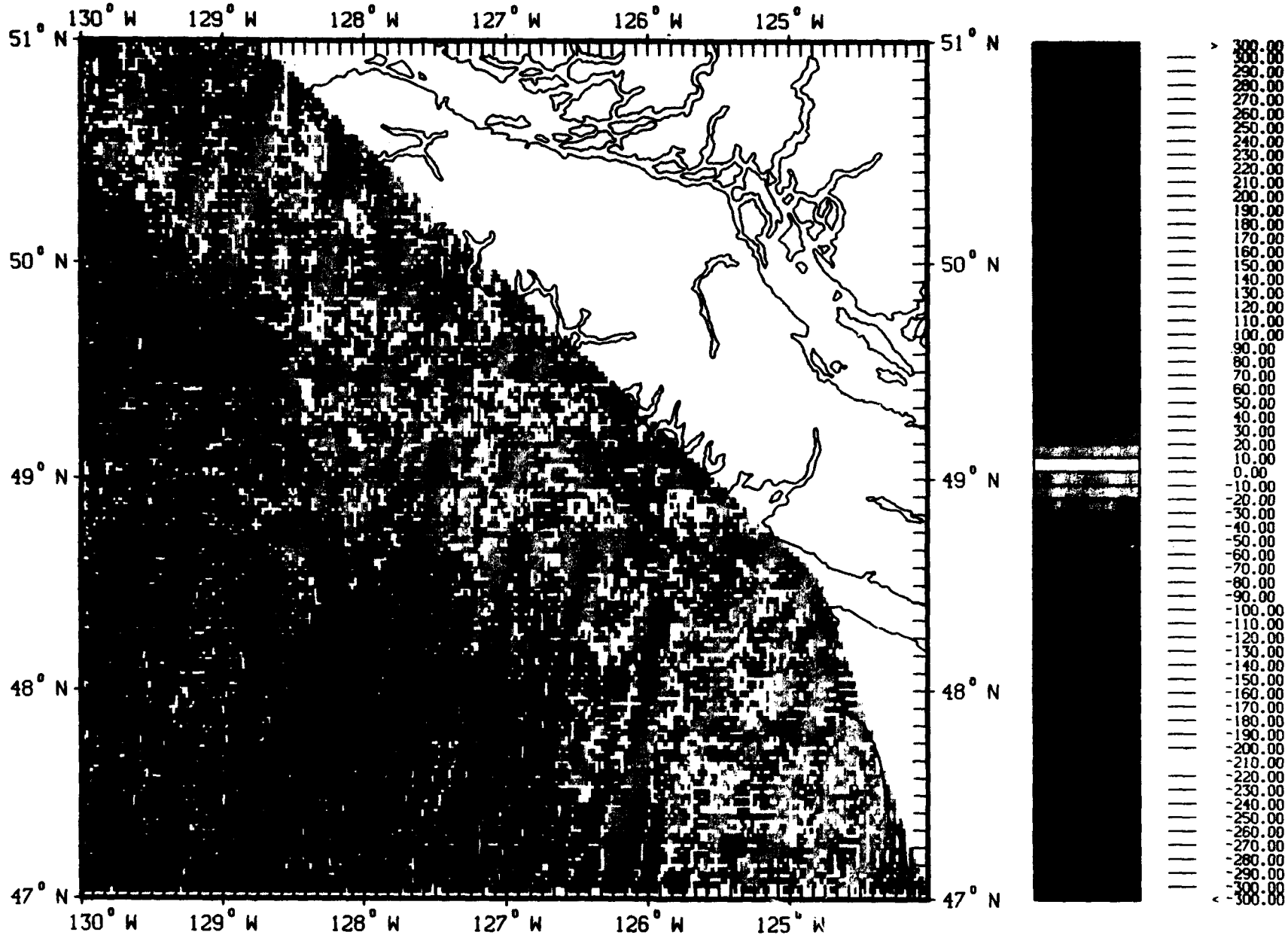

Figure 4f. Juan de Fuca ZZ-Component Magnetic-Field Gradient; Units: nT/km

4. INVERSE MODELING (MAGNETIC DEPTH-TO-SOURCE)

The previously derived rectangular-harmonic model of the northern Juan de Fuca/Explorer plate region is of phenomenological origin since it is based on "observed" survey data. Consequently, the uniformly spaced magnetic component grids of the magnetic-field vector $\mathbf{B}_{obs}(x,y,z)$, depicted in Figures 3a through 3c, and the uniformly spaced magnetic component grids of the magnetic-gradient tensor $\mathcal{B}_{obs}(x,y,z)$, depicted in Figures 4a through 4f, all of which were generated from the model, are also of phenomenological origin and are therefore annotated with the subscript "obs". A single grid location, then, has attached to it three vector-magnetic component observations and nine (five of which are independent) gradient-tensor component observations. We now ask: What is the location, distribution, and equivalent crustal magnetization $\mathbf{M}(\mathbf{r})$ that generates the observed magnetic-vector and magnetic gradient-tensor fields?

The answer to this question draws upon Maxwell's equations, which, for the magnetostatic conditions involved in this problem, reduce to the following Poisson equation, written in Gaussian units, for the scalar magnetic potential $\Phi(\mathbf{r})$:

$$\nabla^2 \Phi(\mathbf{r}) = 4\pi \nabla \bullet \mathbf{M} \tag{41}$$

which has the well-known solution:

$$\Phi(\mathbf{r}) = -\int_{V'} \frac{\nabla' \bullet \mathbf{M}(\mathbf{r})}{|\mathbf{r}-\mathbf{r}'|} \, d^3\mathbf{r}' \tag{42}$$

where $V'(\mathbf{r}')$ is the volume occupied by the magnetized crustal materials and where $\mathbf{r}$ and $\mathbf{r}'$ are

the position vectors from the origin of the rectangular coordinate system to the point of observation $\mathbf{r}(x,y,z)$ and to the location $\mathbf{r}'(x',y',z')$ of the magnetized, oceanic crustal material within the volume V' that generates the observed fields. Through the application of the divergence theorem, as well as through the use of various transformations and identities, all of which are discussed in detail by Quinn and Shiel (1993), eq. (42) can be put into the following, more useful, form:

$$\Phi(\mathbf{r}) = -\nabla \bullet \int_{V'} \frac{\mathbf{M}(\mathbf{r}')}{|\mathbf{r}-\mathbf{r}'|}\, d^3\mathbf{r}' \tag{43}$$

Two assumptions are now made. First, the magnetic-field vector and gradient-tensor components, measured at the point $\mathbf{r}(x,y,z)$, which corresponds to a particular grid location, are generated by magnetized sources in that part of the oceanic crust which is centered directly below the grid location under consideration. Second, the distribution and strength of magnetization in the oceanic crust is slowly varying in the lateral directions away from this grid location, so that within the confines of a few kilometers (e.g., 5 km) of this point, the magnetization may be considered uniform within the volume V' and hence independent of $\mathbf{r}'$. The justification for the first assumption rests on the knowledge that the vector magnetic-field in the far-field approximation varies as R^{-3}, while the magnetic gradient-tensor field varies as R^{-4}, where:

$$R \equiv |\mathbf{r} - \mathbf{r}'| = \sqrt{(x - x')^2 + (y - y')^2 + (z - z')^2} \tag{44}$$

is the distance between a point within the magnetized source volume V' and the point of

observation. The second assumption rests on the knowledge that the peak-to-peak separation of magnetic reversals, at least in the Juan de Fuca region, is on the order of 60 km. Consequently, eq. (43) may be written as:

$$\Phi(\mathbf{r}) = -\mathbf{M} \bullet \nabla \int_{V'} \frac{1}{|\mathbf{r}-\mathbf{r}'|}\, d^3\mathbf{r}' \tag{45}$$

Taking the negative gradient of this potential yields the magnetic-field vector:

$$\mathbf{B}(\mathbf{r}) = \mathbf{M} \bullet \nabla \int_{V'} \nabla\left(\frac{1}{|\mathbf{r}-\mathbf{r}'|}\right) d^3\mathbf{r}' \tag{46}$$

The volume V' may be characterized as a single rectangular prism of dimensions $\lambda_x \times \lambda_y \times \lambda_z$, which were a priori taken to be 5-km x 5-km x 1.5-km on the basis of drill hole data and our knowledge of the far-field behavior of the magnetic field and its gradients. The prism's center is located directly below the known observation point (x_0, y_0), at an unknown source depth z_0, which must be determined from the observed data along with the magnetization vector M, which has constant components $M_1 = M_x$, $M_2 = M_y$, and $M_3 = M_z$.

Using the rectangular-prism geometry, eq. (46) takes the following form in tensor notation:

$$B_\mu(x, y, z) = \Lambda_{\mu\lambda} M^\lambda \tag{47}$$

where Einstein summation over the repeated index λ (one raised and one lowered) is assumed and where the elements of the Λ matrix are given by the relation:

$$\Lambda_{\mu\lambda}(x,y,z) = \frac{\partial}{\partial x^{\mu}}\frac{\partial}{\partial x^{\lambda}}\int_{z_0-\frac{\lambda_z}{2}}^{z_0+\frac{\lambda_z}{2}}\int_{y_0-\frac{\lambda_y}{2}}^{y_0+\frac{\lambda_y}{2}}\int_{x_0-\frac{\lambda_x}{2}}^{x_0+\frac{\lambda_x}{2}}\left(\frac{1}{R}\right)dx'\,dy'\,dz' \tag{48}$$

These matrix elements can be evaluated analytically as discussed by Quinn and Shiel (1993). The results of this evaluation are given in Table 5, where the notation $|_{x',y',z'}$ indicates that the parameters x' , y' , and z' are to be evaluated at their respective upper and lower limits. That is:

$$|_{x',y',z'} \equiv |_{x'=x_0-\frac{\lambda_x}{2}}^{x_0+\frac{\lambda_x}{2}}\,|_{y'=y_0-\frac{\lambda_y}{2}}^{y_0+\frac{\lambda_y}{2}}\,|_{z'=z_0-\frac{\lambda_z}{2}}^{z_0+\frac{\lambda_z}{2}} \tag{49}$$

Consequently, each matrix element in Table 5 has eight terms. Furthermore, it is clear from eq. (48) that the Λ matrix is symmetric. It can also be shown that this matrix has zero trace if the point of observation is outside the volume V' and a trace equal to 4π if the point of observation is inside that volume. This matrix is also a tensor.

Taking the gradient of eq. (47) yields the magnetic-gradient tensor due to a uniformly magnetized prism:

$$\mathcal{B}_{\mu\nu}(x,y,z) = \Lambda_{\mu\lambda/\nu}M^{\lambda} \tag{50}$$

where the derivatives of the Λ matrix elements can also be evaluated analytically and are given in Table 6.

The magnetization of the prism can be formally determined by inverting eq. (47), which yields the result:

Table 5. Elements of the Λ Matrix

$$\Lambda_{11} = + \tan^{-1}\left[\frac{(y-y')(z-z')}{(x-x')R}\right] \Big|_{x',y',z'}$$

$$\Lambda_{12} = - \ln[R + (z - z')] \Big|_{x',y',z'}$$

$$\Lambda_{13} = - \ln[R + (y - y')] \Big|_{x',y',z'}$$

$$\Lambda_{21} = - \ln[R + (z - z')] \Big|_{x',y',z'}$$

$$\Lambda_{22} = + \tan^{-1}\left[\frac{(x-x')(z-z')}{(y-y')R}\right] \Big|_{x',y',z'}$$

$$\Lambda_{23} = - \ln[R + (x - x')] \Big|_{x',y',z'}$$

$$\Lambda_{31} = - \ln[R + (y - y')] \Big|_{x',y',z'}$$

$$\Lambda_{32} = - \ln[R + (x - x')] \Big|_{x',y',z'}$$

$$\Lambda_{33} = + \tan^{-1}\left[\frac{(x-x')(y-y')}{(z-z')R}\right] \Big|_{x',y',z'}$$

Table 6. Derivatives of the Λ Matrix Elements

$$\Lambda_{11/1} = + \frac{1}{R}\left[\frac{(z-z')}{R+(y-y')} + \frac{(y-y')}{R+(z-z')}\right]\Big|_{x',y',z'}$$

$$\Lambda_{11/2} = - \frac{1}{R}\left[\frac{(x-x')}{R+(z-z')}\right]\Big|_{x',y',z'}$$

$$\Lambda_{11/3} = - \frac{1}{R}\left[\frac{(x-x')}{R+(y-y')}\right]\Big|_{x',y',z'}$$

$$\Lambda_{12/1} = - \frac{1}{R}\left[\frac{(x-x')}{R+(z-z')}\right]\Big|_{x',y',z'}$$

$$\Lambda_{12/2} = - \frac{1}{R}\left[\frac{(y-y')}{R+(z-z')}\right]\Big|_{x',y',z'}$$

$$\Lambda_{12/3} = - \frac{1}{R}\Big|_{x',y',z'}$$

$$\Lambda_{13/1} = - \frac{1}{R}\left[\frac{(x-x')}{R+(y-y')}\right]\Big|_{x',y',z'}$$

$$\Lambda_{13/2} = - \frac{1}{R}\Big|_{x',y',z'}$$

$$\Lambda_{13/3} = - \frac{1}{R}\left[\frac{(z-z')}{R+(y-y')}\right]\Big|_{x',y',z'}$$

$$\Lambda_{21/1} = - \frac{1}{R}\left[\frac{(x-x')}{R+(z-z')}\right]\Big|_{x',y',z'}$$

$$\Lambda_{21/2} = - \frac{1}{R}\left[\frac{(y-y')}{R+(z-z')}\right]\Big|_{x',y',z'}$$

$$\Lambda_{21/3} = - \frac{1}{R}\Big|_{x',y',z'}$$

Table 6. Derivatives of the A Matrix Elements (con.)

$$\Lambda_{22/1} = -\frac{1}{R}\left[\frac{(y-y')}{R+(z-z')}\right]\Big|_{x',y',z'}$$

$$\Lambda_{22/2} = +\frac{1}{R}\left[\frac{(z-z')}{R+(x-x')} + \frac{(x-x')}{R+(z-z')}\right]\Big|_{x',y',z'}$$

$$\Lambda_{22/3} = -\frac{1}{R}\left[\frac{(y-y')}{R+(x-x')}\right]\Big|_{x',y',z'}$$

$$\Lambda_{23/1} = -\frac{1}{R}\Big|_{x',y',z'}$$

$$\Lambda_{23/2} = -\frac{1}{R}\left[\frac{(y-y')}{R+(x-x')}\right]\Big|_{x',y',z'}$$

$$\Lambda_{23/3} = -\frac{1}{R}\left[\frac{(z-z')}{R+(x-x')}\right]\Big|_{x',y',z'}$$

$$\Lambda_{31/1} = -\frac{1}{R}\left[\frac{(x-x')}{R+(y-y')}\right]\Big|_{x',y',z'}$$

$$\Lambda_{31/2} = -\frac{1}{R}\Big|_{x',y',z'}$$

$$\Lambda_{31/3} = -\frac{1}{R}\left[\frac{(z-z')}{R+(y-y')}\right]\Big|_{x',y',z'}$$

$$\Lambda_{32/1} = -\frac{1}{R}\Big|_{x',y',z'}$$

$$\Lambda_{32/2} = -\frac{1}{R}\left[\frac{(y-y')}{R+(x-x')}\right]\Big|_{x',y',z'}$$

$$\Lambda_{32/3} = -\frac{1}{R}\left[\frac{(z-z')}{R+(x-x')}\right]\Big|_{x',y',z'}$$

Table 6. Derivatives of the Λ Matrix Elements (con.)

$$\Lambda_{33/1} = -\frac{1}{R}\left[\frac{(z-z')}{R+(y-y')}\right]\Big|_{x',y',z'}$$

$$\Lambda_{33/2} = -\frac{1}{R}\left[\frac{(z-z')}{R+(x-x')}\right]\Big|_{x',y',z'}$$

$$\Lambda_{33/3} = +\frac{1}{R}\left[\frac{(y-y')}{R+(x-x')} + \frac{(x-x')}{R+(y-y')}\right]\Big|_{x',y',z'}$$

$$M^{\lambda} = \bar{\Lambda}^{\lambda\mu} B_{\mu} \tag{51}$$

where the matrix $\bar{\Lambda}$ is the inverse of Λ. Then, inserting this result into eq. (50), yields:

$$\mathcal{B}_{\mu\nu} = \Lambda_{\mu\lambda/\nu} \bar{\Lambda}^{\lambda\sigma} B_{\sigma} \tag{52}$$

This is the main result. It is a nonlinear equation for the magnetic-source-depth z_0, given the "observed" magnetic-field vector and gradient-tensor components at the point (x_0 , y_0). The magnetic-source-depth can be determined by a *nonlinear least-squares minimization of the* chi-square (χ^2) function:

$$\chi^2 = \sum_{\mu=1}^{3} \sum_{\nu=1}^{3} (\mathcal{B}_{\mu\nu} - \mathcal{B}_{\mu\nu\,obs})^2 \tag{53}$$

with respect to z_0. For the Juan de Fuca region, this chi-square function was evaluated as the value of z_0 was varied at 0.1-km intervals from the known bathymetric surface to slightly beyond the estimated Curie depth, which in turn was based on a spherical-harmonic model of heat flow (Pollack and Chapman [1987]). The magnetic-source-depth then corresponds to the minimum value of χ^2. Performing this procedure at each grid point of the survey area yields the magnetic-source-depth of the region as depicted in Figure 5. Clearly defined in this figure, to a high degree of resolution, is the subduction zone just west of Vancouver Island and west of the state of Washington.

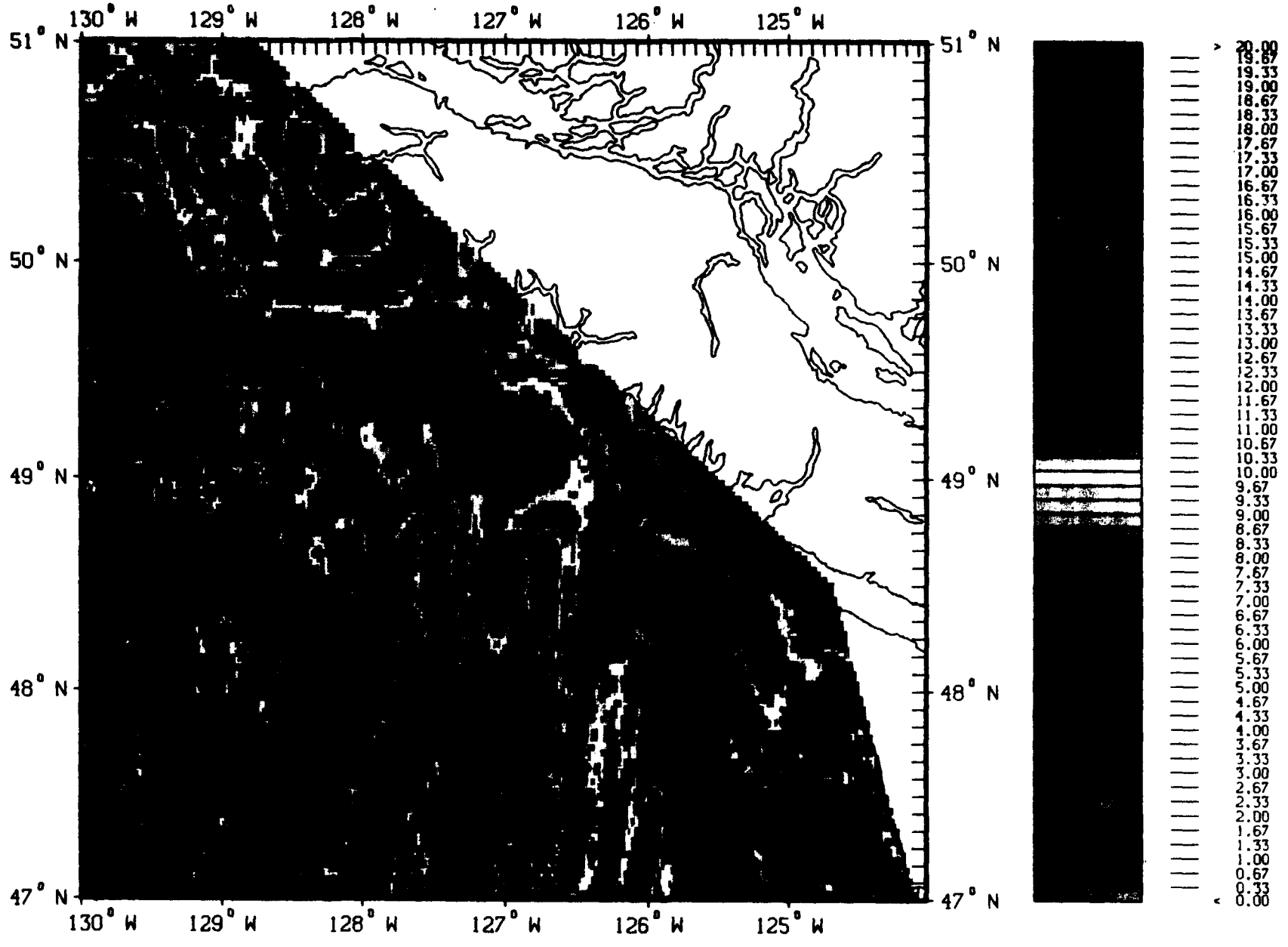

Figure 5. Juan de Fuca Magnetic-Source-Depth; Units: kilometers

Having evaluated the magnetic-source-depth at each grid point, the A matrix and its inverse are, as a consequence, also completely determined at each grid point. This allows the prism magnetization to be evaluated at each grid point through the linear inversion described by eq. (51). The resulting three components of magnetization, which in the Gaussian units used here are expressed in nanoTeslas, at each grid point of the Northern Juan de Fuca/Explorer plate survey region are illustrated in Figures 6a, 6b, and 6c. Figures 7a through 7e are selected magnetic-source-depth profiles of the Z-component magnetization. Figures 7a and 7b are profiles along constant longitude bands, while Figures 7c through 7e are profiles along constant latitude bands. The depths and magnetizations in these figures, though reasonable, are not considered to be absolute, since the a priori assumptions are only approximately true. Secondly, in order to speed up the inversion process an extra "nonessential" constraint was applied to the total magnetization, which limited its value to 4 Amps/meter in SI units. The total magnetization computed during the inversion always reached this limit, indicating that our choice was too low. In the mid to late 1980's, when this work was actually performed, this limit was thought to be reasonable. More recent dredge sampling indicates that the magnetization of younger basalt materials near ridge crests is as much as an order of magnitude greater. The vector components were allowed to vary freely within the limits imposed by the constraint on the total magnetization. The relative depths and magnetizations, so derived, appear at least qualitatively correct but may require appropriate scaling to be quantitatively useful. The fluctuations observed in the depth-to-source magnetization profiles are generally consistent with serpentinization faults generally found at ridge crests (Francis, 1981). For a variety of reasons, we have not found the resources to rerun these computations without this extra, nonessential constraint on the total magnetization as we would prefer to do.

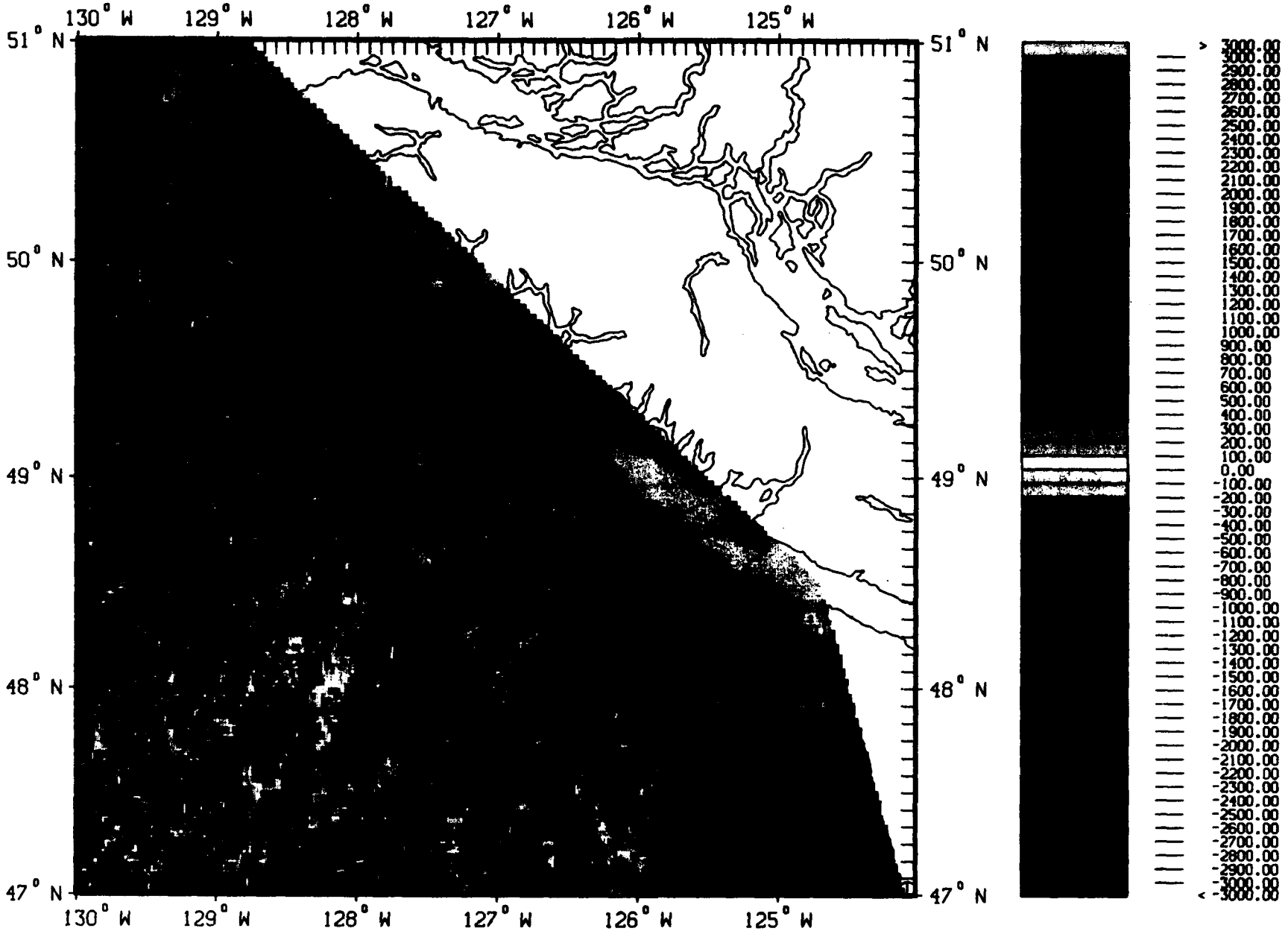

Figure 6a. Juan de Fuca X-Component Magnetization; Units: nT

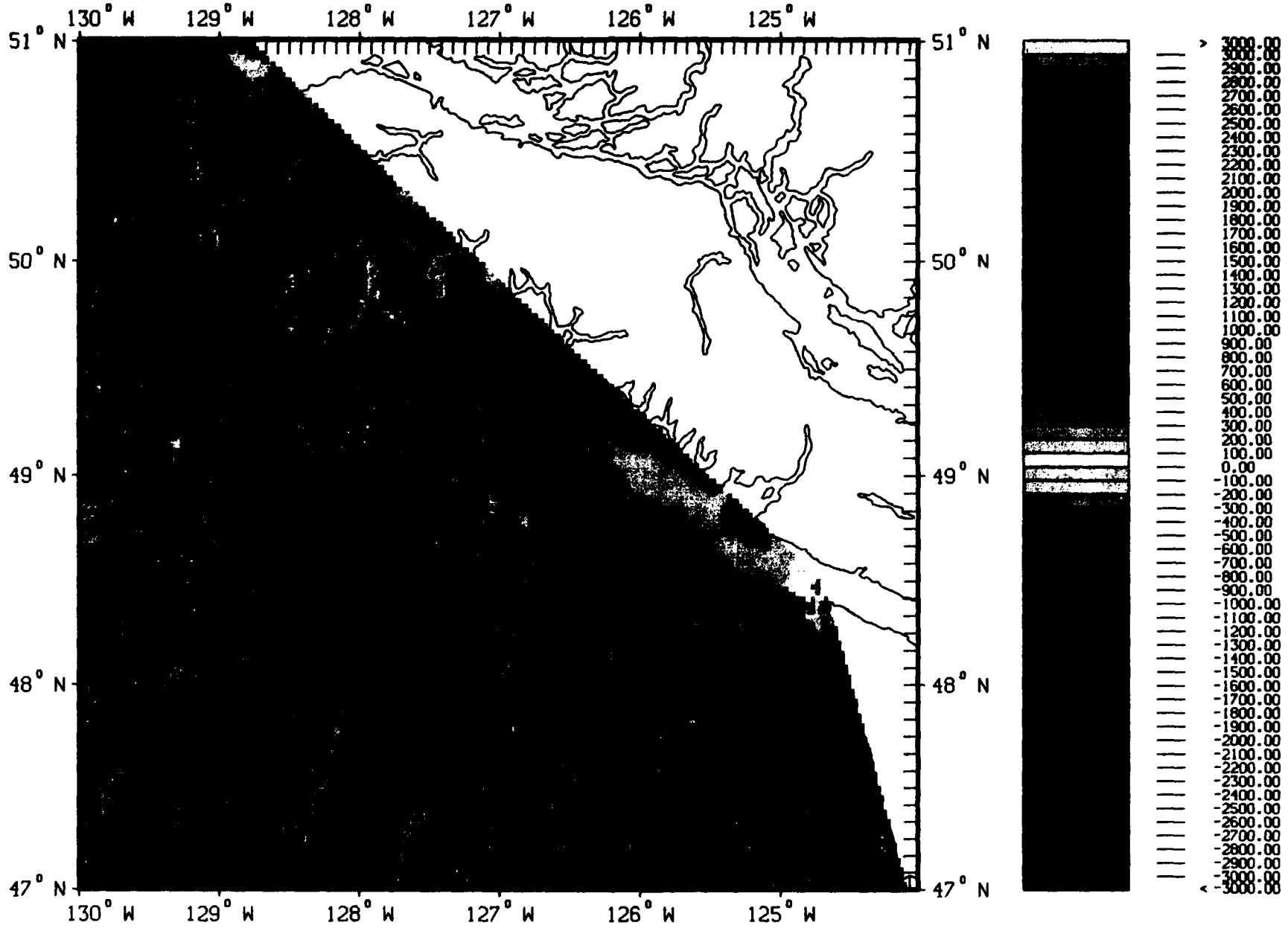

Figure 6b. Juan de Fuca Y-Component Magnetization; Units: nT

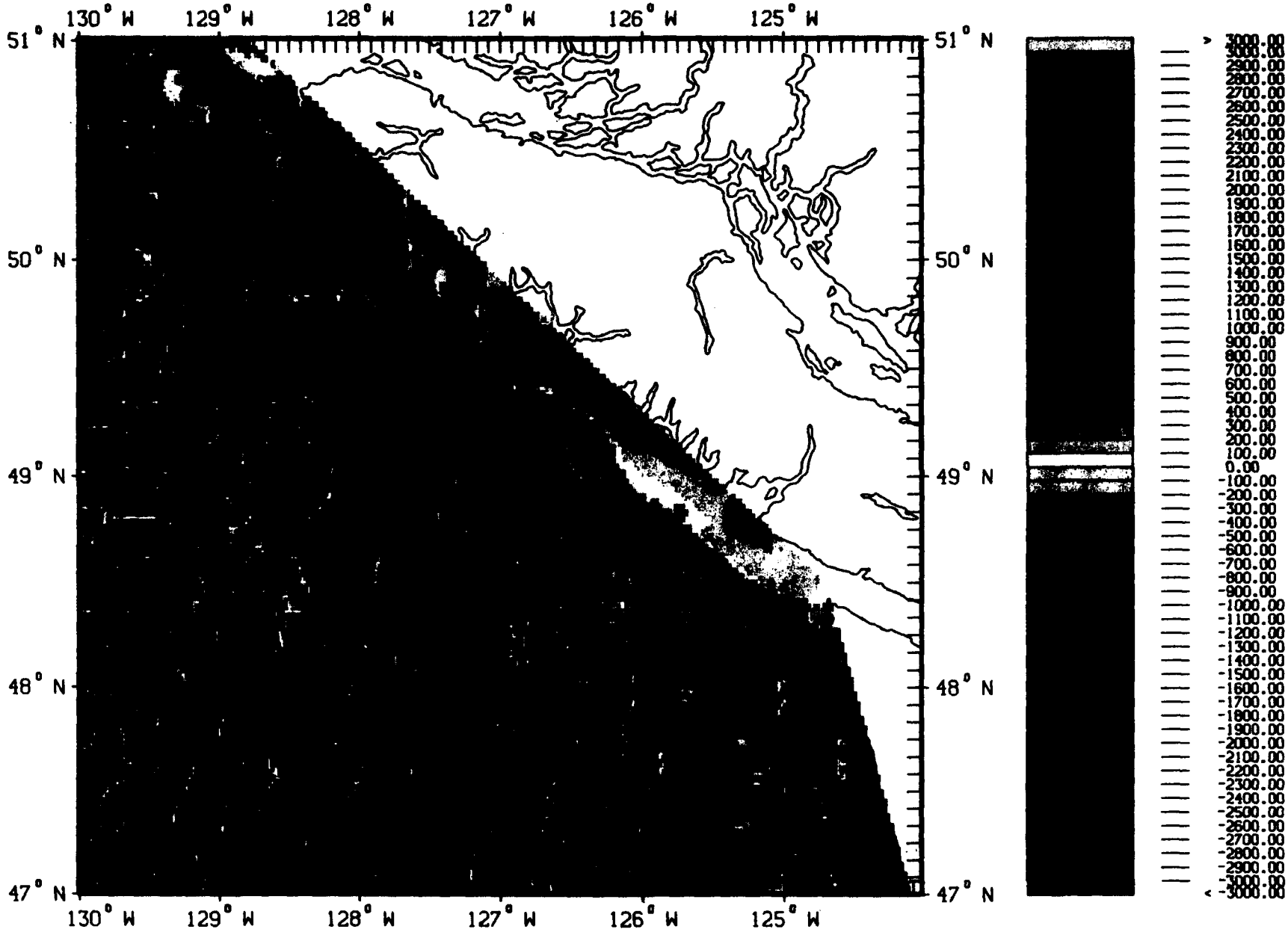

Figure 6c. Juan de Fuca Z-Component Magnetization; Units: nT

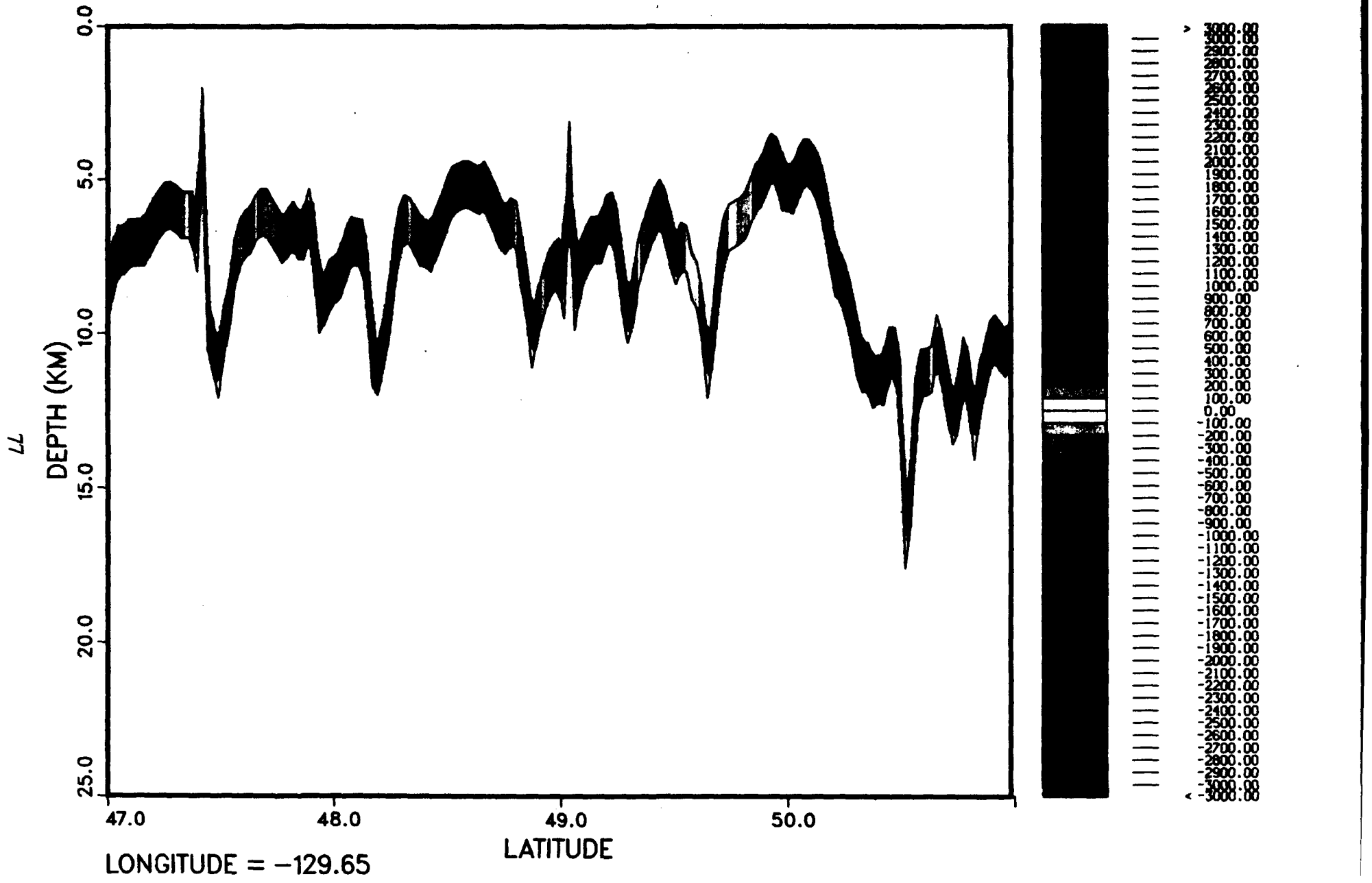

Figure 7a. Juan de Fuca Z-Component Magnetization Profile (nT) Along Longitude 129.65W

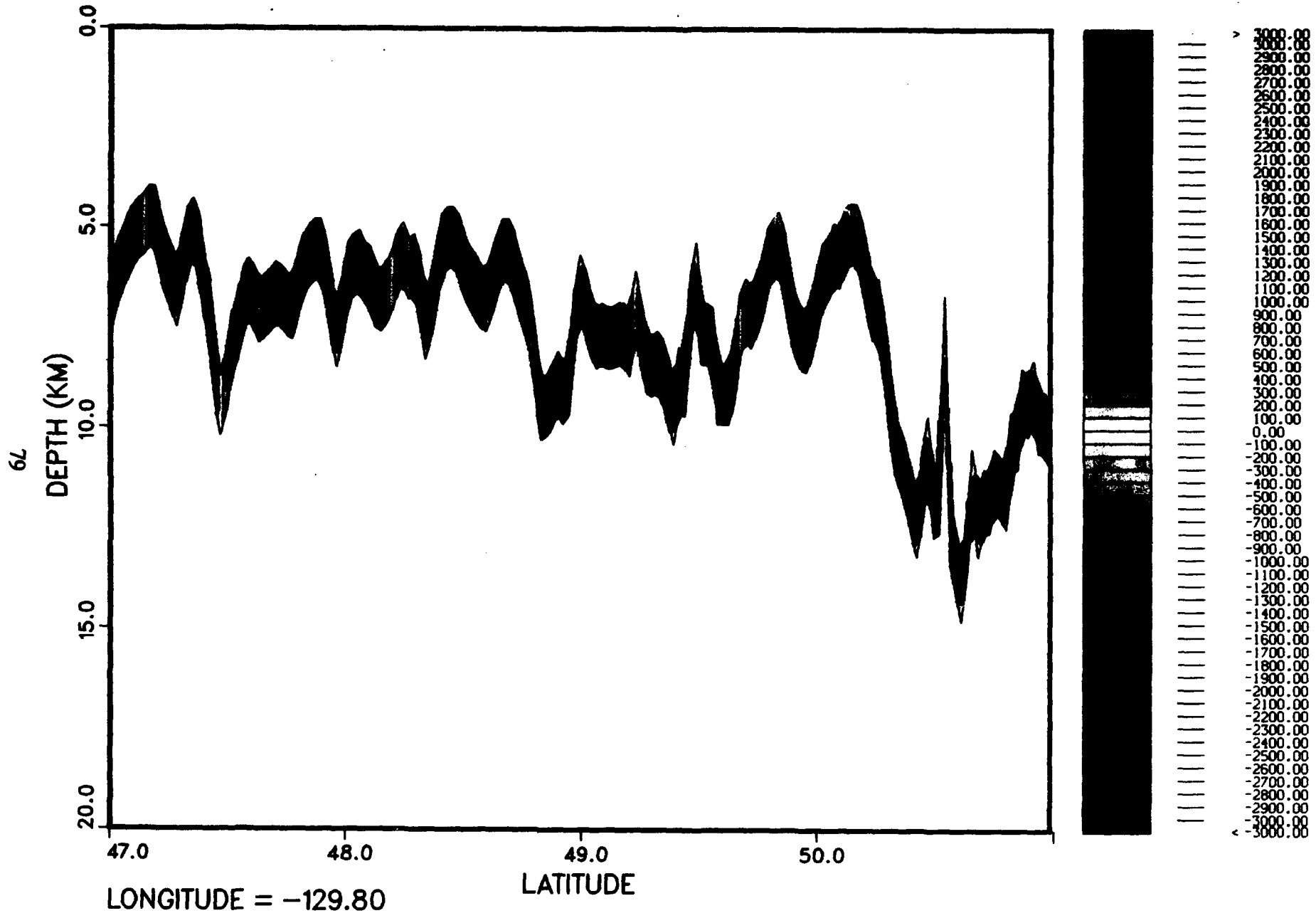

Figure 7b. Juan de Fuca Z-Component Magnetization Profile (nT) Along Longitude 129.80W

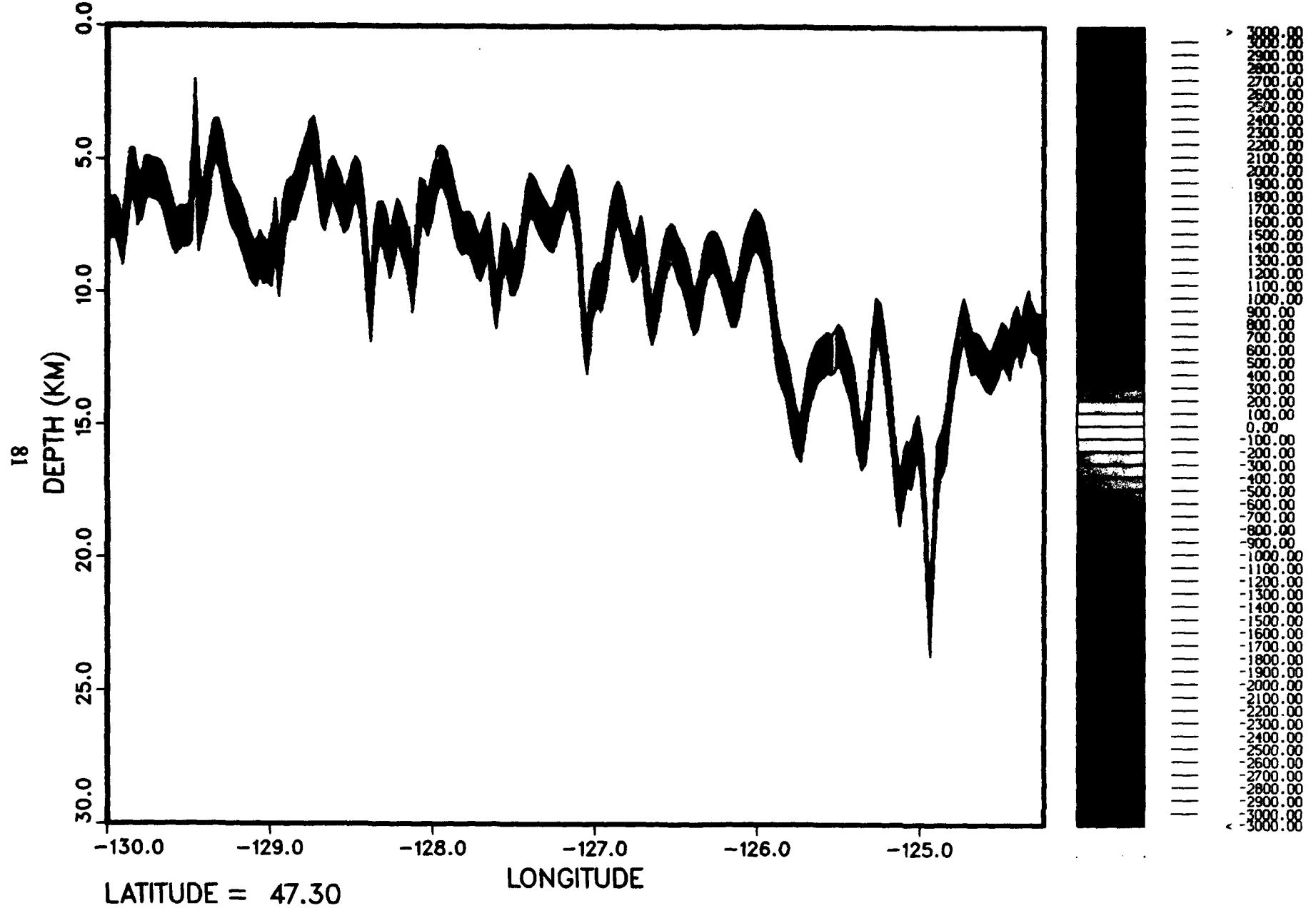

Figure 7c. Juan de Fuca Z-Component Magnetization Profile (nT) Along Latitude 47.30N

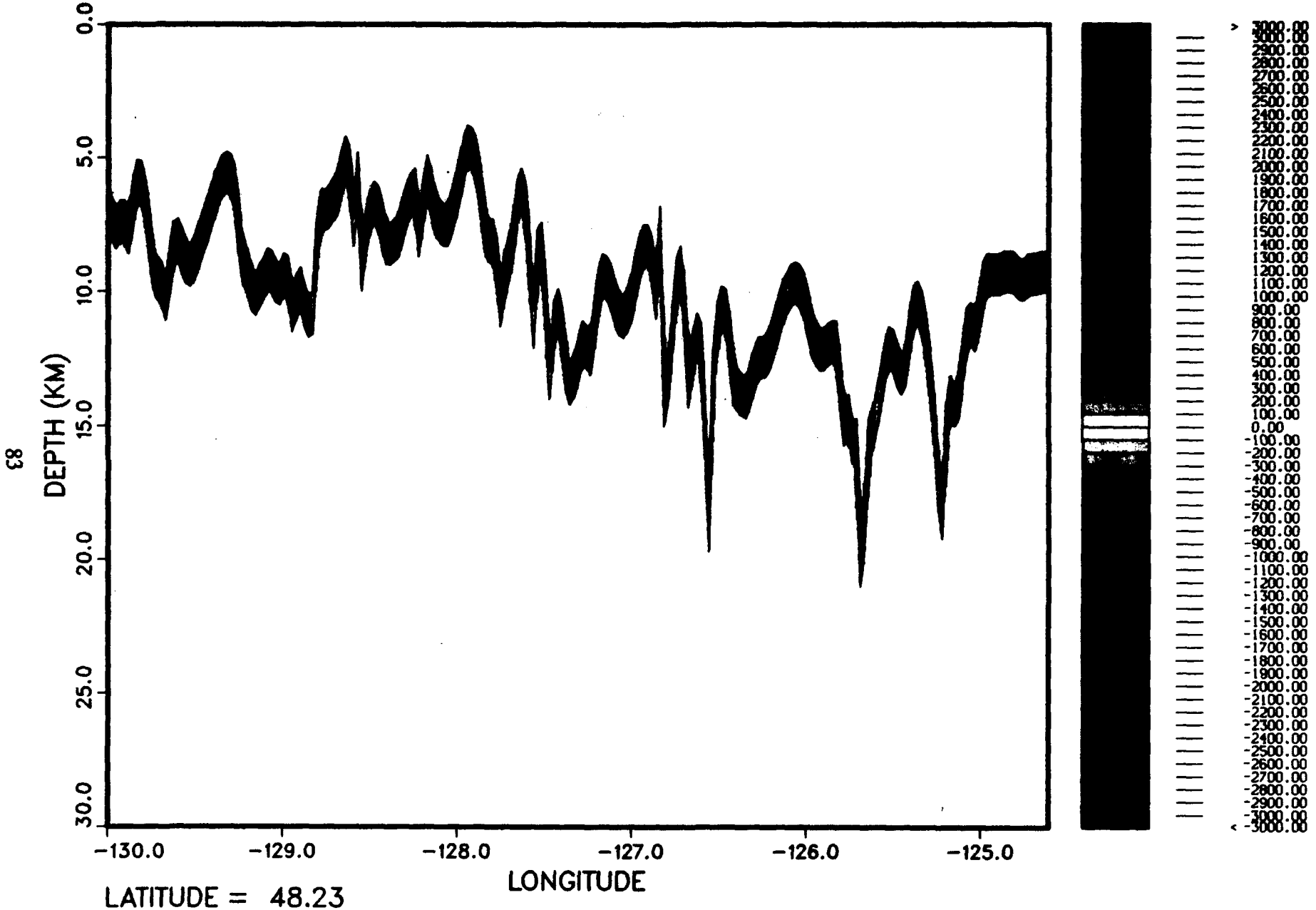

Figure 7d. Juan de Fuca Z-Component Magnetization Profile (nT) Along Latitude 48.23N

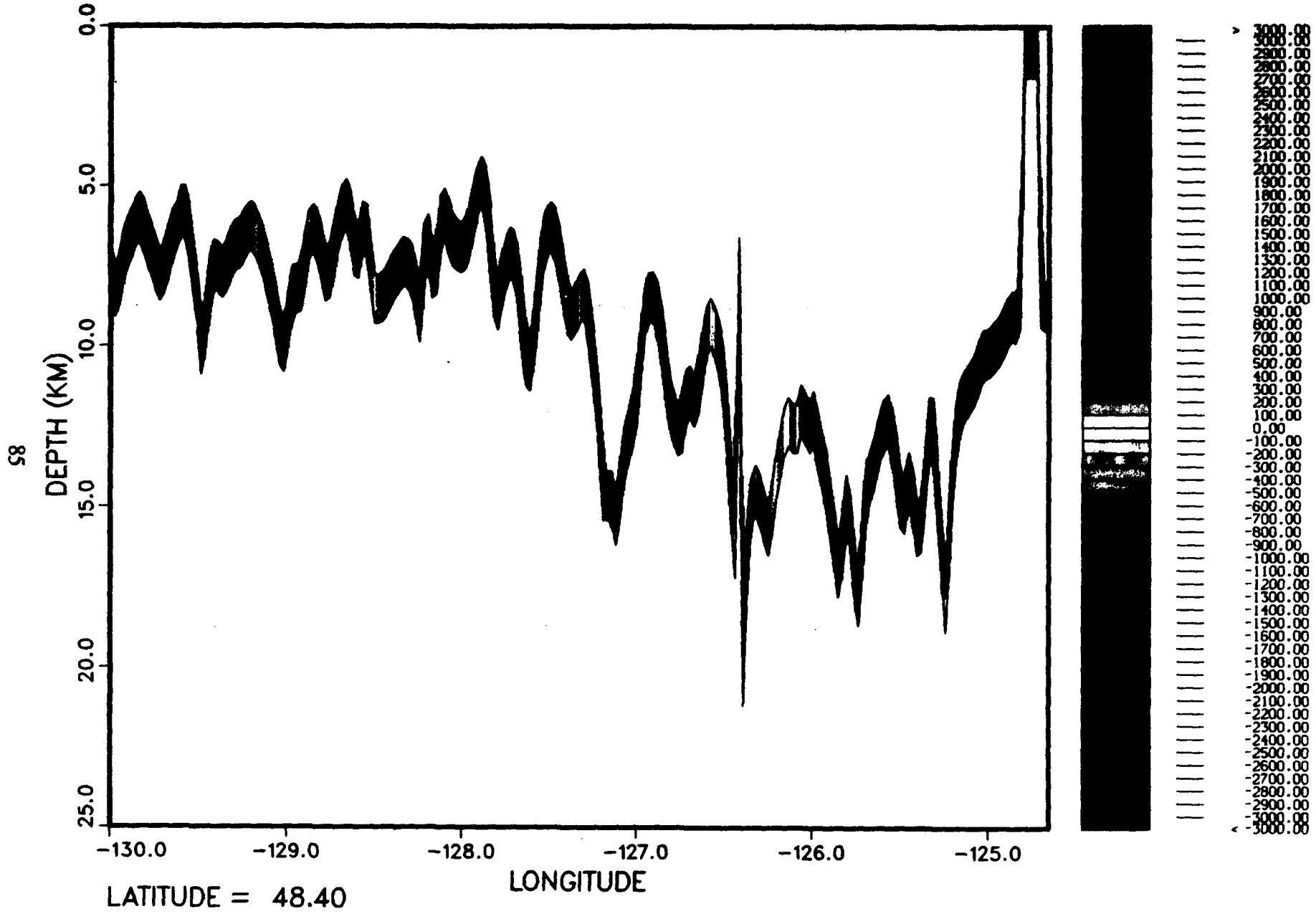

Figure 7e. Juan de Fuca Z-Component Magnetization Profile (nT) Along Latitude 48.40N

5. COMMENTS ON NONUNIQUENESS

The inverse geopotential modeling problem is notoriously nonunique. That is, for a given set of magnetic-field survey measurements, many distributions of magnetization may be found that can reproduce the observed magnetic field. This is true regardless of the accuracy of the magnetic-field measurements. The way around this difficulty is to make reasonable assumptions based on a priori information that may restrict the possible source geometry and reduce the number of possible unknown parameters. In the present case, we assumed a rectangular-prism geometry based on the idea that the lateral magnetic character of a large oceanic region does not, as a rule, change drastically over the course of a few kilometers. Furthermore, this choice of geometry was based on drill hole and other data which indicated that the largest source of magnetization in the ocean crust is confined to the basalt layer. The choice of the rectangular-prism geometry still left nine parameters to determine, three components of magnetization, three coordinates specifying the center location of the prism, and three prism dimension parameters. Then, given only the vector magnetic-field measurements (i.e., no gradient data) as is frequently the case, defining the elements c_j , j = 1,2,...6 to correspond to the prism parameters (x_0, ... λ_x, λ_y, and λ_z) and neglecting magnetic-field measurement errors, we find that a variation of the parameters c_j in eq. (47) yields:

$$\delta B_\mu = \frac{\partial \Lambda_{\mu\lambda}}{\partial c_j} M^\lambda \delta c_j + \Lambda_{\mu\lambda} \delta M^\lambda = 0 \tag{54}$$

which implies:

$$\delta M^\lambda = - \overline{\Lambda}^{\lambda\mu} \frac{\partial \Lambda_{\mu\sigma}}{\partial c_j} M^\sigma \delta c_j \tag{55}$$

Equations (54) and (55) state that without any further constraints on the geometric parameters c_j, any variation in one or more of these parameters can be offset by a compensating variation in the magnetization, which will leave the magnetic field unchanged. So, without further constraints, the solution is ambiguous. This ambiguity is eliminated by first demanding that the prism be centered directly below the particular grid point under consideration. This means that $\delta c_1 = \delta c_2 = 0$. Further noting that the magnetic field falls off sharply with distance from the source, a cutoff length to the lateral dimensions of the prism can be imposed (we used 5 km), so that $\delta c_4 = \delta c_5 = 0$. Drill hole, seismic, and other data indicate that in the ocean, the primary source of the crustal-generated magnetic field is located in the basalt layer which is approximately 1.5-km thick. Using this value for c_6 sets $\delta c_6 = 0$. This leaves the source depth $c_3 = z_0$, as the remaining undetermined geometric parameter, which, without further constraining information, will still lead to a nonunique solution. The required new information comes from our knowledge of the magnetic gradient. A variation of the geometric parameters in eq. (52), again ignoring measurement errors, so that $\delta \mathcal{B}_{\mu\nu} = 0$, yields:

$$\left\{ \frac{\partial \Lambda_{\mu\lambda/\nu}}{\partial c_j} \bar{\Lambda}^{\lambda\sigma} B_\sigma + \Lambda_{\mu\lambda/\nu} \frac{\partial \bar{\Lambda}^{\lambda\sigma}}{\partial c_j} B_\sigma \right\} \delta c_j = 0 \tag{56}$$

Since $\delta c_j = 0$ for $j \neq 3$, eq. (56) reduces to:

$$\left\{ \frac{\partial \Lambda_{\mu\lambda/\nu}}{\partial c_3} \bar{\Lambda}^{\lambda\sigma} B_\mu + \Lambda_{\mu\lambda/\nu} \frac{\partial \bar{\Lambda}^{\lambda\sigma}}{\partial c_3} B_\sigma \right\} \delta c_3 = 0 \tag{57}$$

This is actually a set of 9 equations, 5 of which are independent. Each of these equations

implies that the source depth uncertainty $\delta c_3 = \delta z_0 = 0$, since the term within the brackets is not zero in general.

Thus, the method used to determine the magnetizations and source depths yields a unique solution at least to the extent that the *arbitrarily* imposed constraints on the lateral prism dimensions are satisfied. The largest source of error in this procedure results from the assumption that just one magnetic source exists beneath a specified grid location. Actually, weaker sources exist at shallower depths. The characteristics of these weaker sources can be determined through an iteration process which removes the magnetic fields generated by magnetizations obtained through the inversion procedure from the original survey-generated rectangular grids of crustal magnetic-field and gradient-tensor residuals. This process may be repeated until the residual magnetic-field vector is of the order of the measurement errors associated with the survey. For each iteration, the same uniqueness arguments apply, as do the provisos.

As a final note, it should be kept in mind that we could have minimized eq. (53) with respect to the lateral dimensions of the prism (λ_x and λ_y) as well as the prism's source depth z_0. This removes the arbitrary nature of the lateral dimensions at the expense of considerable amounts of computer time. However, this would not resolve the ambiguity problem since, as the above exercise indicates, for any particular source depth, an infinite set of lateral dimension combinations will satisfy the minimization problem. The addition of one more physically reasonable constraint would resolve the ambiguity. For example, one could also simultaneously demand that the prism volume be a minimum. The physical basis for this particular constraint is rather dubious and no other physically reasonable constraints were found. So, this approach was not taken.

REFERENCES

Adler, R., M. Bazin and M. Schiffer; **Introduction to General Relativity**, Mc Graw-Hill Book Company, New York (1975)

Alldredge, L. R.; Rectangular Harmonic Analysis Applied to the Geomagnetic Field, *Journal of Geophysical Research*, Vol. 86, No. B4, pp. 3021-3026 (1981)

Alldredge, L. R.; Geomagnetic Local and Regional Harmonic Analyses, *Journal of Geophysical Research*, Vol. 87, No. B3, pp. 1921-1926 (1982)

Applegate, T. B. Jr.; Volcanic and Structural Morphology of the South Flank of Axial Volcano, Juan de Fuca Ridge: Results From a Sea Marc I Side Scan Sonar Survey, *Journal of Geophysical Research*, Vol. 95, No. B8, pp. 12765-12783 (1990)

Botros, M. and H. P. Johnson; Tectonic Evolution of the Explorer - Northern Juan de Fuca Region From 8 Ma to the Present, *Journal of Geophysical Research*, Vol. 93, No. B9, pp. 10421-10437 (1988)

Cain, J. C., S. J. Hendricks, R. A. Langel, and W. V. Hudsen; A Proposed Model for the International Geomagnetic Reference Field-1965, *Journal of Geomagnetism and Geoelectricity*, Vol. 19, No. 4, pp. 335-355 (1967)

Campbell, W. H; An Introduction to Quiet Daily Geomagnetic Fields, *Pure and Applied Geophysics*, Vol. 131, pp. 316-331 (1989a)

Campbell, W. H.; The Regular Geomagnetic Field Variations During Quiet Solar Conditions, in **Geomagnetism**, Vol. 3, ch. 6, pp. 386-460, edited by J. A. Jacobs, Academic Press, San Diego, CA (1989b)

Campbell, W. H. and E. R. Schiffmacher; Upper Mantle Electrical Conductivity for Seven Subcontinental Regions of the Earth, *Journal of Geomagnetism and Geoelectricity*, Vol. 40, pp. 1387-1406 (1988a)

Campbell, W. H. and E. R. Schiffmacher; Quiet Ionospheric Currents of the Southern Hemisphere Derived from Geomagnetic Records, *Journal of Geophysical Research*, Vol. 93, pp. 933-944 (1988b)

Campbell, W. H, E. R. Schiffmacher, and H. W. Kroehl; Global Quiet Day Field Variation Model WDCA/SQ1, *EOS Transactions*, Vol. 70, No. 5, pp. 66 (1989)

Coleman, R. J.; Project MAGNET High-Level Vector Survey Data Reduction, *NASA Conference Publication*, No. 3153, pp. 215-248 (1992)

Elvers, D., K. Potter, D. Seidel, and J. Morley, I. D. O. E. Survey Seamap Plate BGM-1-71, *NOAA Environmental Data Service*, Washington D. C. (1974)

Finn, C.; Geophysical Constraints on Washington Convergent Margin Structure, *Journal of Geophysical Research*, Vol. 95, No. B12, pp. 19533-19546 (1990)

Francis, T. J. G.; Serpentinization Faults and their Role in the Techtonics of Slow Spreading Ridges, *Journal of Geophysical Research*, Vol. 86, No. B12, pp. 11616-11622 (1981)

Harris, R. A., H. M. Iyer, and B. Dawson; Imaging the Juan de Fuca Plate Beneath Southern Oregon Using Teleseismic P-Wave Residuals, *Journal of Geophysical Research*, Vol. B12, pp. 19879-19889 (1991)

Hildebrand, J. A., J. M. Stevenson, P. T. C. Hammer, M. A. Zumberge, and R. L. Parker; A Seafloor and Sea Surface Gravity Survey of Axial Volcano, *Journal of Geophysical Research*, Vol. 95, No. B8, pp. 12751-12763 (1990)

Karsten, J. L. and J. R. Delaney; Hot Spot - Ridge Crest Convergence in the Northeast Pacific, *Journal of Geophysical Research*, Vol. 94, No. B1, pp. 700-712 (1989)

Langel, R. A. and R. H. Estes; The Near-Earth Magnetic Field at 1980 Determined from Magsat Data, *Journal of Geophysical Research*, Vol. 90, No. B3, pp. 2495-2509 (1985)

Morton, J. L., N. H. Sleep, W. R. Normark, and D. H. Tompkins; Structure of the Southern Juan de Fuca Ridge From Seismic Reflection Records, *Journal of Geophysical Research*, Vol. 92, No. B11, pp. 11315-11326 (1987)

Pollack, H. N. and D. S. Chapman; Global Heat Flow Revisited, *Presented at the International Association of Geodesy and Geophysics*, Vancouver, BC (1989)

Quinn, J. M. and D. L. Shiel; A Unified Approach to Geopotential Field Modeling, *Technical Report No. 308*, Naval Oceanographic Office, Stennis Space Center, MS (1993)

Raff, A. D. and R. G. Mason; Magnetic Survey off the West Coast of North America, 40^0 Latitude to 50^0 N Latitude, *Geological Society of America Bulletin*, Vol. 72, pp. 1267-1270 (1961)

Rasmussen, J. and E. Humphreys; Tomographic Image of the Juan de Fuca Plate Beneath Washington and Western Oregon Using Teleseismic P-Wave Travel Times, *Geophysical Research Letters*, Vol. 15, No. 12, pp. 1417-1420 (1988)

Rhodes, J. M., C. Morgan, and R. A. Liias; Geochemistry of Axial Seamount Lavas: Magmatic Relationship Between the Cobb Hotspot and the Juan de Fuca Ridge, *Journal of Geophysical Research*, Vol., 95, No. B8, pp. 12713-12733 (1990)

Tivey, M. A. and H. P. Johnson; The Magnetic Structure of Axial Seamount, Juan de Fuca Ridge, *Journal of Geophysical Research*, Vol. 95, No. B8 (1990)

White, D. J. and R. M. Clowes; Shallow Crustal Structure Beneath the Juan de Fuca Ridge from 2-D seismic Refraction Tomography, *Geophysical Journal International*, Vol. 100, pp. 349-367 (1990)

DISTRIBUTION LIST

NAVY	
Chief of Naval Operations	5
Chief of Naval Research	2
David Taylor Naval Ship Research and Development Center	2
Dept. of the Navy, Submarine Combat and Weapons Systems	1
Mine Countermeasure Group Two	1
Mine Warfare Command	1
Marine Corps Research, Development and Acquisitions Command	1
Naval Air Systems Command	1
Naval Air Test Center	2
Naval Air Warfare Center	4
Naval Avionics Center	1
Naval Coastal Systems Center	2
Naval Command Control and Ocean Surveillance Center	2
Naval Oceanographic Office N342, N4312	150
Naval Oceanographic Office N2, N25CL, N25CP, N5	4
Naval Oceanography Command	3
Naval Oceanography Command Detachments (All)	50
Naval Ocean Systems Center	3
Naval Postgraduate School	3
Naval Research Laboratory, Washington DC	6
Naval Research Laboratory Detachment SSC	6
Naval Sea Systems Command	3
Naval Surface Warfare Center, White Oak	4
Naval Surface Weapons Center, Dahlgren	3
Naval Surface Weapons Laboratory Detachment, White Oak	3
Naval Technical Intelligence Center	1
Naval Undersea Warfare Center Detachment, San Diego	1
Naval Underwater Systems Center Detachment, New London Laboratory	1
Naval Underwater Systems Center Detachment, Newport Laboratory	1
Naval Underwater Warfare Center	3
Naval Weapons Center	1
Office of Advanced Technology	2
Office of Naval Research, Washington DC	3
Office of Naval Research Detachment SSC	2
Office of Naval Technology	1
Space and Naval Warfare Systems Command PMW-182, PMW-185	2
USMC 3rd. R.P.V. Experimental Brigade	2
U. S. Naval Academy (Nimitz Library)	1
AIR FORCE	
Air Force Institute of Technology	1
Air Force Office of Scientific Research	1

Pacific Missile Test Center	3
Rome Research Laboratory	2
U. S. Air Force Academy (Technical Library)	1
USAF Air Warfare Center	1
USAF Hq., Electronics Systems Division	1
USAF Phillips Laboratory, AFGL	2
USAF Phillips Laboratory, Kirkland AFB	1
USAF Weapons and Tactics Center	1
ARMY	
Harry Diamond Laboratory (Technical Library)	1
U. S. Army Combat Systems Test Activity	2
U. S. Army Research Laboratory	3
U. S. Military Academy (Technical Library)	1
DOD	
DARPA, Submarine Technology Program	1
DARPA, Nuclear Monitoring Program	1
Defense Mapping Agency, Aerospace Center	4
Defense Mapping Agency, GPS-NAVSTAR JPO	1
Defense Mapping Agency Headquarters	4
Defense Mapping Agency, Hydrographic and Topographic Center	3
Defense Mapping Agency, Systems Center	3
Defense Mapping School	2
Defense Technical Information Center	2
Los Alamos National Laboratory	2
National Security Agency	1
Sandia National Laboratory (Technical Library)	1
NON-DOD	
Australian Geological Survey	1
British Geological Survey	2
Bedford Institute of Oceanography (Technical Library)	1
Canadian Defence Research Establishment Pacific	2
Colorado School of Mines, Center for Potential Field Studies	2
Geological Survey of Canada, Geophysics Division	3
Geological Survey of Canada, Atlantic Geoscience Centre	3
Geological Survey of Canada, Pacific Geoscience Centre	3
Geothe Universitat, Institute Fur Meteorologie und Geophysik	3
Hatfield Marine Science Center	3
Istituto Nazionale Di Geofisica	1
IZMIRAN	2
Institut de Physique du Globe de Paris	2
Johns Hopkins University, Applied Physics Laboratory	1
Lawrence Livermore Laboratory (Technical Library)	1
McGill University, Dept. of Earth and Planetary Sciences	1

NASA, Geodynamics Branch	5
NOAA, NGDC	3
NOAA, Pacific Marine Environment Laboratory	2
Oregon State University, College of Oceanography	1
Purdue University, Dept. of Earth and Atmospheric Sciences	1
Raytheon Corporation	2
Royal Australian Navy, Maritime Hq.	2
SACLANT ASW Research Centre	2
Scripps Institution of Oceanography	2
Stanford University, Dept. of Geological Sciences	1
Tracor, Incorporated	3
U. S. Geological Survey, Denver	5
U. S. Geological Survey, Menlo Park	2
University of Cantebury, Dept. of Geology	1
University of Michigan, Dept. of Geophysics	1
University of Rhode Island, Graduate School of Oceanography	1
University of Sydney, School of Mathematics and Statistics	1
University of Toronto, Dept. of Physics, Geophysics Laboratory	1
University of Washington, School of Oceanography	2
Woods Hole Oceanographic Institution	2